International Journal of Thermofluids 24 (2024) 100843

Contents lists available at ScienceDirect

International Journal of Thermofluids

journal homepage: www.sciencedirect.com/journal/international-journal-of-thermofluids

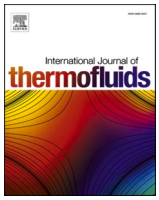

Numerical analysis of free convection under the influence of radiation and inclined MHD in a triangular cavity filled with hybrid nanofluid and a porous fin

Ahmed M. Hassan [a], Mohammed Azeez Alomari [b,c,*], Qusay H. Al-Salami [d], Farah Q.A. Alyousuf [e], Faris Alqurashi [f], Mujtaba A. Flayyih [g]

[a] Department of Mechanical Engineering, University of Al-Qadisiyah, Al-Qadisiyah, 58001, Iraq
[b] Department of Mechanical Engineering, University of Al-Qadisiyah, Ad-Diwaniyah, 58001, Iraq
[c] College of Engineering, University of Warith Al-Anbiyaa, Karbala, Iraq
[d] Department of Business Administration, College of Administrative and Financial Sciences, Cihan University, Erbil, Iraq
[e] Department of Computer Network, College of Engineering and Computer Science, Lebanese French University, Erbil, Kurdistan Region, Iraq
[f] Mechanical Engineering Dept., College of Engineering, University of Bisha, Bisha, Saudi Arabia
[g] Biomedical Engineering Department, College of Engineering and Technologies, Al-Mustaqbal University, Hillah, Iraq

ARTICLE INFO

Keywords:
Rayleigh numbers
Hybrid nanofluid
Porous media
Darcy-forchheimer
Entropy generation
Radiation
Inclined MHD

ABSTRACT

This study presents a novel investigation into the thermal behavior of a hybrid nanofluid ($MgO - Ag - H_2O$) in natural convection around a porous fin in a triangular enclosure under the influence of radiation and magnetohydrodynamic effects. The research uniquely combines these complex phenomena, addressing a significant gap in the literature. This configuration has potential applications in advanced solar thermal collectors, electronic cooling systems for high-power devices, and compact heat exchangers in various industries. The main objectives are to understand how various parameters influence heat transfer and fluid flow behavior and to optimize the design for enhanced thermal performance. The study considers a range of variables including Rayleigh number ($10^3 - -10^6$), Hartmann number (0 – 50), Aspect ratio (0.3 – 0.6), radiation parameters ($Rd = 1 - -5$, $\lambda = 1 - 5$), and volume concentration (0- 0.05), which have been numerically analyzed using the finite element method (FEM). The findings reveal that increasing the Darcy number (*Da*) enhances heat transfer at low Rayleigh numbers ($Ra = 10^3$,10^4). However, at higher *Ra* ($Ra = 10^6$), the impact of *Da* becomes more complex, with a critical *Da* beyond which heat transfer efficiency decreases due to an increase in flow resistance. The nanoparticle volume concentration plays a vital role, as higher concentrations lead to improved heat transfer efficiency, especially at higher Ra, through enhanced thermal conductivity and thermal dispersion. The length of the porous fin greatly impacts fluid flow patterns and heat transfer rates, with longer fins creating more complex flow patterns, promoting enhanced heat transfer and stronger thermal plumes. Thermal radiation, represented by the radiation parameters (*Rdand*λ), significantly influences both the heat transfer rate and the convective flow patterns within the enclosure. This study also incorporates a comprehensive entropy generation analysis, providing novel insights into system irreversibilities and optimization potential. The entropy analysis reveals the complex interplay between various parameters and their impact on system efficiency, offering valuable guidance for designing high-performance thermal management systems.

1. Introduction

Optimizing the performance and efficiency of engineering systems is a crucial endeavor, and a key aspect of this is the investigation of heat transfer and fluid flow characteristics. One area of particular interest is the study of natural convection, a phenomenon that plays a significant role in thermal management processes. Free convection, which is a widespread and important phenomenon in many applications, is caused by temperature gradients and resulting differences in densities [1]. Heat

* Corresponding author.
E-mail addresses: ahmed.mohammed.hassan@qu.edu.iq (A.M. Hassan), mohammed.hasan@qu.edu.iq (M.A. Alomari), qusay.hameed@cihanuniversity.edu.iq (Q.H. Al-Salami), frhalyousuf@lfu.edu.krd (F.Q.A. Alyousuf), fars421@hotmail.com (F. Alqurashi), mujtaba_abdulkadhim@mustaqbal-college.edu.iq (M.A. Flayyih).

https://doi.org/10.1016/j.ijft.2024.100843

Available online 1 September 2024

Nomenclature

Be	Bejan number
Cp	Specific heat, (J. kg-1. K-1)
Da	Darcy number
Bo	Magnetic induction (Tesla)
g	Gravitational acceleration, (m.s-2)
Ha	Hartmann number
K	Permeability of the porous medium
k	Thermal conductivity, (W.m-1. K-1)
L	Fin length, (m)
Nu	Nusselt number
p	Pressure, (Pa)
pˆ’	Non-dimensional pressure
Pr	Prandtl number
Ra	Rayleigh number
Rd	Radiation parameter
S	Entropy generation (J.kg-1.K-1)
T	Temperature, (K)
T’	Dimensionless temperature
t	Fin thickness, (m)
u	Velocity component x-direction, (m.s-1)
uˆ’	Non-dimensional velocity component X-direction
v	Velocity component y-direction, (m.s-1)
vˆ’	Non-dimensional velocity component Y-direction
W	Width of triangular enclosure, (m)
x	Cartesian x-coordinates, (m)
xˆ’	Non-dimensional X-coordinates
y	Cartesian y-coordinates, (m)
yˆ’	Non-dimensional Y-coordinates

Greek symbols

μ	Dynamic viscosity, (kg. m-1. s-1)
α	Thermal diffusivity, (m2. s-1)
β	Thermal expansion coefficient, (K-1)
ε	Porosity
γ	Angle of inclination of the magnetic field
ν	Kinematic viscosity, (m2.s-1)
λ	Heat generation parameter
σ	Electrical conductivity (S.m-1)
σ_B	Stefan-Boltzmann’s constant (W.m-2. K-4)
ξ	Non-dimensional variables
ρ	Density, (kg.m-3)
φ	Solid volume fraction
Ψ	Absolute stream function

Subscripts

av	Average
c	Cold
eff	Effected
f	Fluid (pure water)
h	Hot
hnf	Hybrid nano fluid
L	Local
po	Porous media

Abbreviation

AR	Aspect ratio

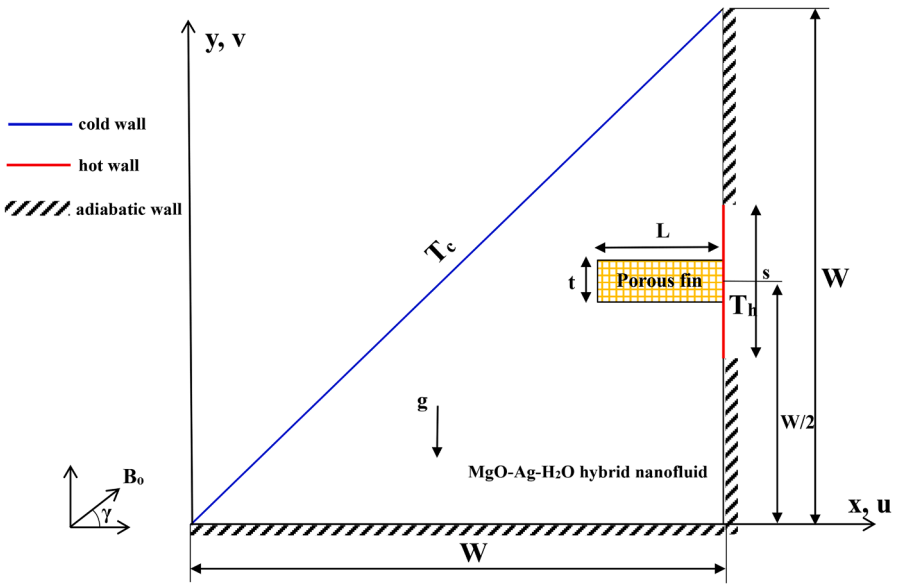

Fig. 1. Physical geometry of the model.

exchangers are a popular application where free convection is dominant, and heat transfer can be enhanced by increasing the surface area [2]. There are numerous other important applications, such as cooling of electronics [3–6], renewable energy storage [7,8], and even highly sensitive and critical applications such as nuclear reactors [9]. Furthermore, free convection plays an important role in air conditioning systems, one of the most common engineering applications [10,11]. These applications motivate researchers to conduct further research in this area to identify the parameters that affect this phenomenon.

Table 1
Thermophysical properties of the fluid and two MgO and Ag types of nanoparticles [60,68,69].

Properties	Water	MgO	Ag
$c_p(J.kg^{-1}.K^{-1})$	4179	879	235
$k(W.m^{-1}.K^{-1})$	0.613	30	429
$\alpha(m^2.s^{-1})$	1.47×10^{-7}	95.3×10^{-7}	174×10^{-3}
$\beta(K^{-1})$	21×10^{-5}	33.6×10^{-6}	$5.4^{*} \times 10^{-5}$
$\rho(kg.m^{-3})$	997.1	3580	10,500
$\mu(kg.m^{-1}.s^{-1})$	8.9×10^{-4}	–	–

Table 2
Effective thermophysical properties of hybrid nanofluid.

Hybrid nanofluid properties	Relations	Source
Density (ρ)	$\rho = (1-\varphi)\rho_f + \varphi_{MgO}\rho_{MgO} + \varphi_{Ag}\rho_{Ag}$ (31)	[68]
Thermal expansion coefficient (ρβ)	$(\rho\beta) = (1-\varphi)(\rho\beta)_f + \varphi_{MgO}(\rho\beta)_{MgO} + \varphi_{Ag}(\rho\beta)_{Ag}$ (32)	[68]
Specific heat capacity (ρc_p)	$(\rho c_p)_{hnf} = (1-\varphi)(\rho c_p)_f + \varphi_{MgO}(\rho c_p)_{MgO} + \varphi_{Ag}(\rho c_p)_{Ag}$ (33)	[68]
Thermal conductivity (k)	$\frac{k_{hnf}}{k_f} = \frac{0.1747 \times 10^5 + \varphi_{hnf}}{0.1747 \times 10^5 - 0.1498 \times 10^6\varphi_{hnf} + 0.1117 \times 10^7\varphi_{hnf}^2 + 0.1997 \times 10^8\varphi_{hnf}^3}$ (34) $0 \le \varphi_{hnf} \le 0.03$	[60]
Thermal diffusivity (α)	$\alpha_{hnf} = \frac{k_{hnf}}{(\rho c_p)_{hnf}}$ (35)	[68]
Viscosity (μ)	$\frac{\mu_{hnf}}{\mu_f} = \left(1 + 32.795\varphi_{hnf} - 7214\varphi_{hnf}^2 + 714600\varphi_{hnf}^{3)} - 0.1941 \times 10^8\varphi_{hnf}^4\right)$ (36) $0 \le \varphi_{hnf} \le 0.02$	[60]

Table 3
Grid independence test for average Nusselt number and maximum stream function.

Grid size	Number of element	Nu_{av}	% Error	ψ_{max}	% Error
G1	177	1.7545	…	0.1596	…
G2	275	1.8223	3.8643	0.1623	1.6534
G3	384	1.8755	2.9193	0.1640	1.0597
G4	645	1.9462	3.7696	0.1653	0.8047
G5	966	1.9728	1.3667	0.1658	0.2781
G6	1483	2.0163	2.2049	0.1671	0.8141
G7	4466	2.1224	5.2621	0.1678	0.4307
G8	**12,299**	**2.192**	**3.2793**	**0.1682**	**0.1965**
G9	15,405	2.1933	0.0593	0.1684	0.1129

The performance properties of base fluids, such as water, can be improved by adding nanoparticles in different concentrations [12–15]. Researchers have found that heat transfer can be improved by adding these nanoparticles due to the enhancement of the thermophysical properties of the base fluid [16–18]. Moreover, researchers have recently started to mix more than one type of nanoparticle to create what are called hybrid nanofluids, which provide more heat transfer enhancement than single nanoparticles [19–21]. Guedri et al. [22] studied the influence of introducing $MWCNT - Fe_3O_4/water$ into a cavity filled with porous material. Their results showed that adding the nanoparticles enhanced free convection for all Rayleigh number values. Mehryan et al. [23] studied the addition of different hybrid nanofluids, specifically $Al_2O_3 - Cu/water$, into a porous cavity that was heated from the left wall and cooled from the right wall. The authors observed a noticeable enhancement in heat transfer due to adding these nanoparticles, and the heat transfer increased with increasing hybrid concentration. Similar results were found by Huda et al. [24] who investigated adding $Ag - MgO/water$ into a square porous cavity. Mahboobtosi et al. [25] used ternary hybrid nanofluids composed of MoS_2, Cu, and Ag to improve heat transfer around a cylinder. Haque and Alam [26] studied the effect of a periodic magnetic field on heat transfer in a hybrid nanofluid consisting of $Al_2O_3 - Cu/water$ placed inside a rectotrapezoidal cavity. Islam et al. [27] used sensitivity analysis to predict the effect of $Cu - TiO_2/water$ hybrid nanofluids on the thermal performance of a prismatic-shaped enclosure.

Furthermore, porous media, which are permeable materials, can be utilized for different purposes such as enhancing heat transfer. This enhancement is achieved by using porous foam, which can improve the thermal conductivity of the fluid [1,28,29]. Researchers have utilized porous media in different ways, where in some cases it fills the entire cavity [30,31] and in other cases is partially used [32–34]. Natural convection in a cavity filled with porous material was studied, using numerical analysis, by Geridonmez et al. [35]. A range of Darcy numbers was examined in this paper, and based on its results, the authors stated that heat transfer enhanced as the Darcy number increased. Moreover, some researchers studied the use of porous fins for free convection and heat transfer enhancement [36–38], concluding that there was an enhancement in heat transfer when using porous fins.

On the other hand, heat transfer can be significantly influenced by magnetohydrodynamic forces, which is why many studies examined this

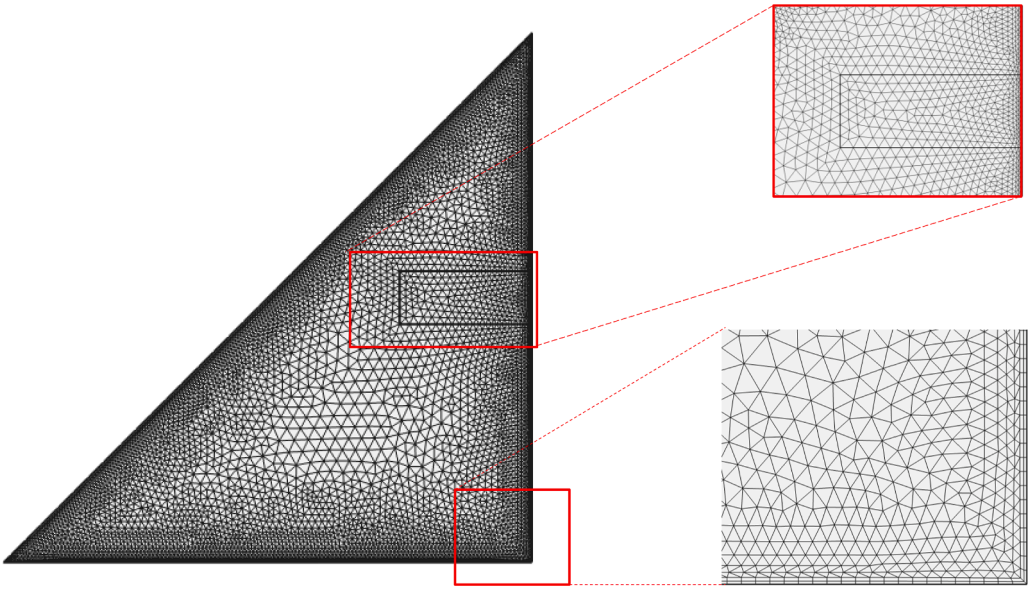

Fig. 2. The meshing of the computational domain.

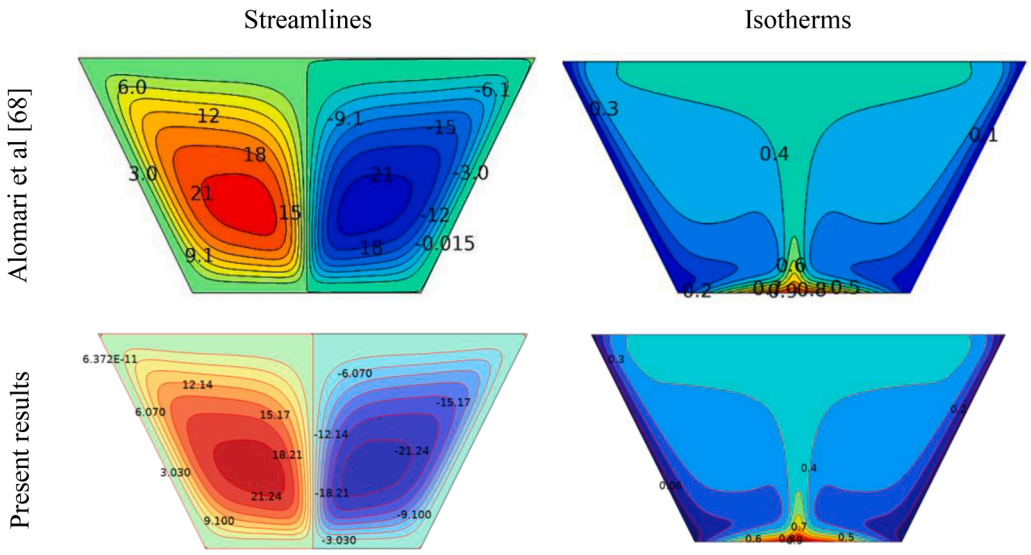

Fig. 3. Comparison of isotherms and streamlines between present study and Alomari et al. [68] results.

variable to understand its influence on convective heat transfer [39–42]. Mirzaei et al. [40] investigated the influence of applying different strengths of MHD in a circular cavity with different obstacles. According to this study, applying MHD reduced the strength of convection in the cavity. A study conducted by Ahmad et al. [43] involved a numerical investigation into the impact of magnetohydrodynamic forces on a cavity with four fins attached to its four corners. The results confirmed the prior findings, demonstrating that the magnetohydrodynamic (MHD) phenomenon reduces both convection and mass transfer. Alomari et al. [32] studied the effect of a porous block on the heat transfer process, in the presence of a nanofluid and an inclined magnetic field. Recently, researchers have shown increased interest in studying the effect of magnetic fields on heat and mass transfer processes. Some studies, such as [44–48], investigated the effect of a constant magnetic field in magnitude and direction, while other studies, such as [49–52], examined the effect of a periodic magnetic field. Additionally, some studies focused on other types of fields, such as the electric field (Electrohydrodynamic), as seen in [53–55]. The effect of radiation on convective heat transfer has been studied recently in many works, such as [56–59].

This research aims to study free convection in a triangular cavity filled with a hybrid nanofluid ($MgO - Ag - H_2O$) and attached to a porous fin, under the combined influence of MHD and radiation. The study examines a range of variables such as Ra, Ha, ϕ, AR, Rd, $and\lambda$. The novelty of the case considered, as well as the important variables examined, can enhance our understanding of heat transfer. This configuration has several potential applications in various fields of engineering and technology. In Solar Thermal Collectors, the triangular shape resembles certain solar thermal collector designs. The porous fin could serve as a heat absorption element, while the nanofluid enhances heat transfer efficiency. This setup could be used to study and optimize the performance of novel solar thermal systems. For electronic cooling systems, the model could represent a section of an advanced cooling system for electronic components. The porous fin might act as a heat sink, while the nanofluid and magnetic field provide enhanced heat dissipation capabilities. This is particularly relevant for high-power electronics and data center cooling applications. This study presents a novel investigation into the thermal behavior of a hybrid nanofluid ($MgO - Ag - H_2O$) in natural convection around a porous fin within a triangular enclosure, uniquely combining the effects of radiation and magnetohydrodynamics. Our research addresses a significant gap in the literature by examining the interplay of these complex phenomena.

2. Problem formulation

2.1. Physical domain

The current model, with its most important physical boundary conditions, is well illustrated in Fig. 1. The geometry consists of a right-angled triangular enclosure filled with a hybrid nanofluid, $MgO - Ag - H_2O$. The vertical wall includes a heated surface at a temperature of T_h along a length $s = 0.5W$, on which a porous fin is mounted. The inclined surface is cooled to T_c. The lower wall and the remaining portion of the vertical wall are insulated. The base of the triangular enclosure is equal in length to its height, both equal to W. The fin has dimensions of L in length and t in thickness, and the aspect ratio ($AR = t/L$) is varied from 0.3 to 0.6 in the current study.

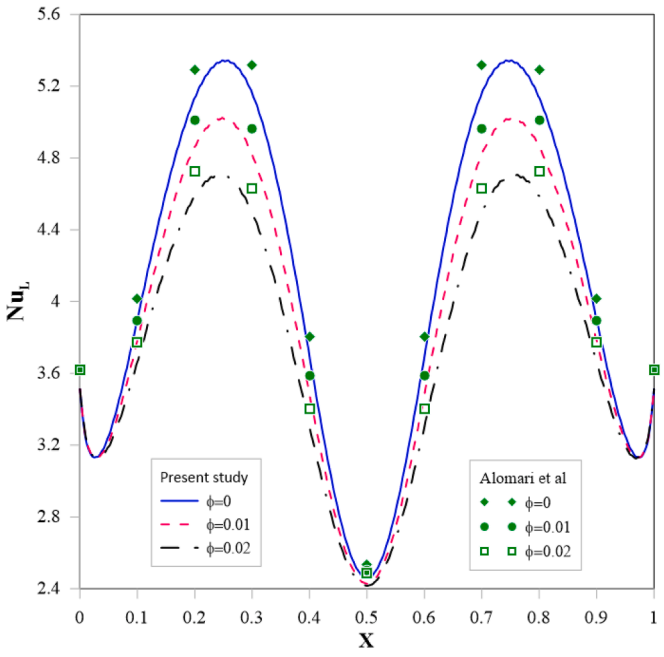

Fig. 4. Local Nusselt number distribution comparison between present study and Alomari et al. [68] results.

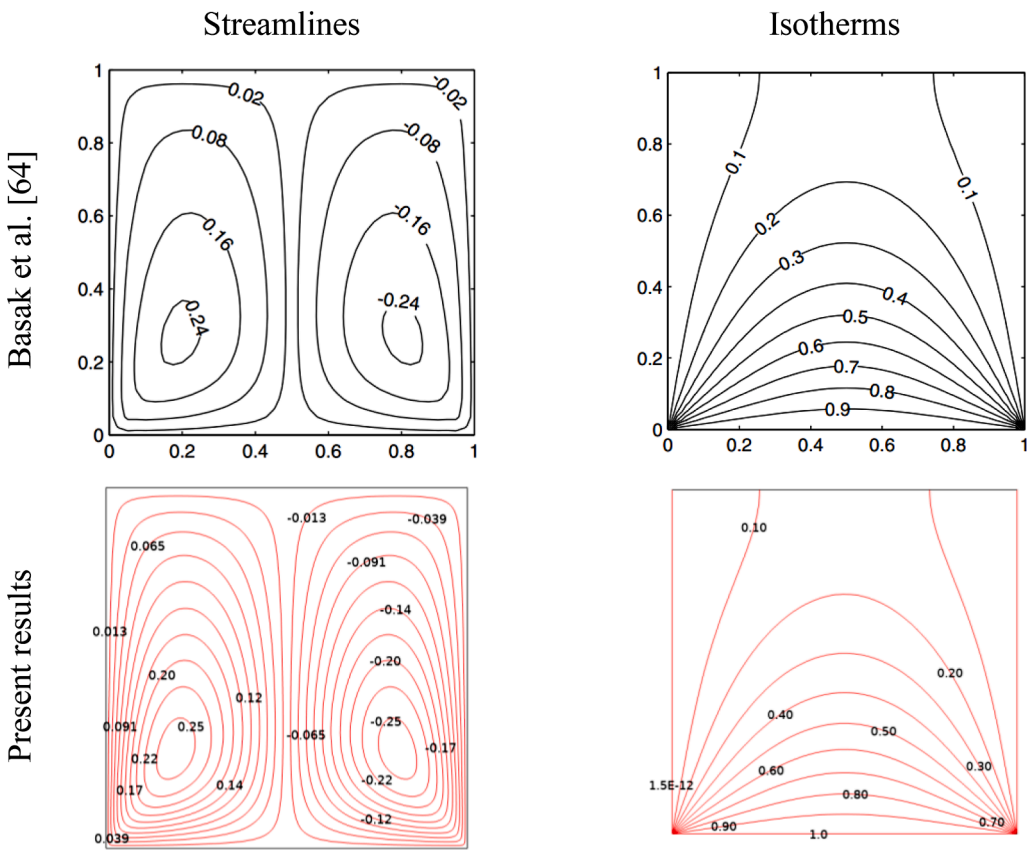

Fig. 5. Comparison of isotherms and streamlines between present study and Basak et al. [64] results.

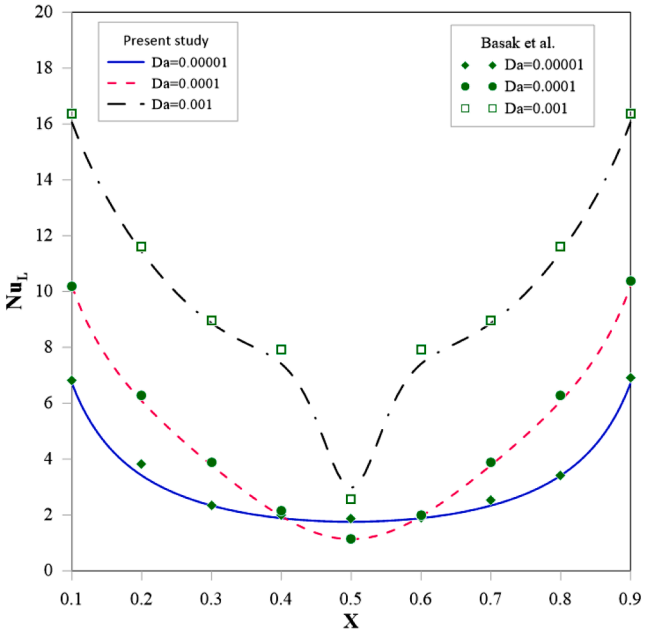

Fig. 6. Local Nusselt number distribution comparison between present study and Basak et al. [64] results.

2.2. Governing equations

To analyze the thermal behavior of a hybrid nanofluid undergoing natural convection around a porous fin in a triangular enclosure, several governing equations need to be considered. The following equations describe the fluid flow and heat transfer phenomena involved:

-For the hybrid nanofluid, the continuity equation governing the conservation of mass is expressed as follows [60]:

$$\frac{\partial u_{nf}}{\partial x}+\frac{\partial v_{nf}}{\partial y}=0 \tag{1}$$

The Navier-Stokes equations describe the conservation of momentum and can be written as [43,60]:

$$u_{nf}\frac{\partial u_{nf}}{\partial x}+v_{nf}\frac{\partial u_{nf}}{\partial y}=-\frac{1}{\rho_{nf}}\frac{\partial p}{\partial x}+\nu_{nf}\left(\frac{\partial^2 u_{nf}}{\partial x^2}+\frac{\partial^2 u_{nf}}{\partial y^2}\right)+\frac{\sigma_{nf}B_o{}^2}{\rho_{nf}}\sin(\gamma)\left(v_{nf}\cos(\gamma)-u_{nf}\sin(\gamma)\right) \tag{2}$$

$$u_{nf}\frac{\partial v_{nf}}{\partial x}+v_{nf}\frac{\partial v_{nf}}{\partial y}=-\frac{1}{\rho_{nf}}\frac{\partial p}{\partial y}+\nu_{nf}\left(\frac{\partial^2 v_{nf}}{\partial x^2}+\frac{\partial^2 v_{nf}}{\partial y^2}\right)+g\frac{(\rho\beta_T)_{nf}}{\rho_{nf}}(T-T_c)+\frac{\sigma_{nf}B_o{}^2}{\rho_{nf}}\cos(\gamma)\left(u_{nf}\sin(\gamma)-v_{nf}\cos(\gamma)\right) \tag{3}$$

The energy equation accounts for the conservation of energy and is given by [58]:

$$u_{nf}\frac{\partial T_{nf}}{\partial x}+v_{nf}\frac{\partial T_{nf}}{\partial y}=\alpha_{nf}\left(\frac{\partial^2 T_{nf}}{\partial x^2}+\frac{\partial^2 T_{nf}}{\partial y^2}\right)-\left(\frac{\partial q_{rx}}{\partial x}+\frac{\partial q_{ry}}{\partial y}\right)+\frac{Q}{(\rho c_p)_{nf}}(T-T_c) \tag{4}$$

-For porous fin, the continuity equation governs the conservation of mass and is expressed as follows [61,62]:

$$\frac{\partial u_{po}}{\partial x}+\frac{\partial v_{po}}{\partial y}=0 \tag{5}$$

To account for the presence of the porous fin, the Darcy-Forchheimer model is employed, with Forchheimer's inertia term neglected [63].

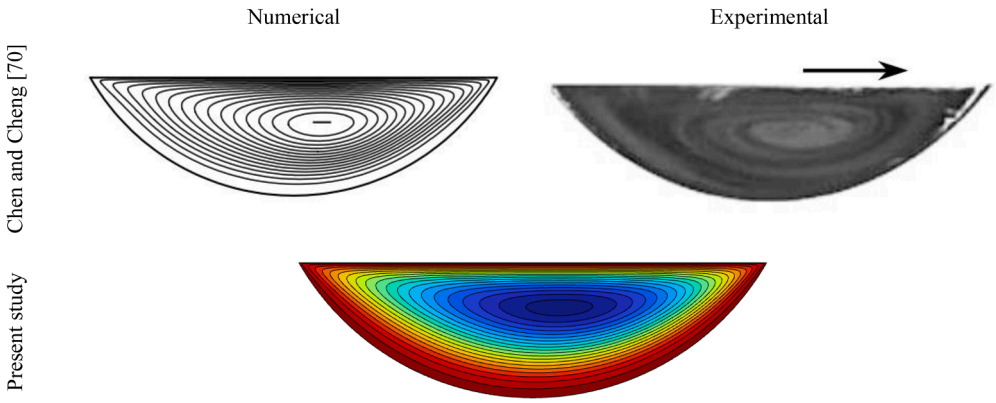

Fig. 7. Validation of streamlines results with experimental and numerical rustles of Chen and Cheng Results [70].

This model incorporates the effects of fluid flow resistance within the porous medium and is given by [64,65]:

$$u_{po}\frac{\partial u_{po}}{\partial x}+v_{po}\frac{\partial u_{po}}{\partial y}=-\frac{1}{\rho_{nf}}\frac{\partial p}{\partial x}+\nu_{nf}\left(\frac{\partial^2 u_{po}}{\partial x^2}+\frac{\partial^2 u_{po}}{\partial y^2}\right)-\frac{\mu_{nf}}{\rho_{nf}}\frac{u_{po}}{K}+\frac{\sigma_{po}{B_o}^2}{\rho_{po}}\sin(\gamma)\left(v_{po}\cos(\gamma)-u_{po}\sin(\gamma)\right) \quad (6)$$

$$u_{po}\frac{\partial v_{po}}{\partial x}+v_{po}\frac{\partial v_{po}}{\partial y}=-\frac{1}{\rho_{nf}}\frac{\partial p}{\partial y}+\nu_{nf}\left(\frac{\partial^2 v_{po}}{\partial x^2}+\frac{\partial^2 v_{po}}{\partial y^2}\right)+g\frac{(\rho\beta_T)_{nf}}{\rho_{nf}}(T-T_c)-\frac{\mu_{nf}}{\rho_{nf}}\frac{v_{po}}{K}+\frac{\sigma_{po}{B_o}^2}{\rho_{po}}\cos(\gamma)\left(u_{po}\sin(\gamma)-v_{po}\cos(\gamma)\right) \quad (7)$$

The energy equation accounts for the conservation of energy and is given by:

$$u_{po}\frac{\partial T_{po}}{\partial x}+v_{po}\frac{\partial T_{po}}{\partial y}=\frac{k_{eff}}{\rho_{nf}cp_{nf}}\left(\frac{\partial^2 T_{po}}{\partial x^2}+\frac{\partial^2 T_{po}}{\partial y^2}\right)-\left(\frac{\partial q_{rx}}{\partial x}+\frac{\partial q_{ry}}{\partial y}\right)+\frac{Q}{(\rho c_p)_{nf}}(T-T_c) \quad (8)$$

It is [assumed] that the boundary layer has a high opacity and that the Rosseland [56] approximation accurately describes radiative heat transfer. Therefore, for an optically thick boundary layer (meaning it has a high level of absorption), the radiative heat flux, as indicated by Uddin et al. [57], can be defined as:

$$q_{rx}=\frac{16{T_c}^3}{3\beta}\frac{\partial T}{\partial x},q_{ry}=\frac{16{T_c}^3}{3\beta}\frac{\partial T}{\partial y} \quad (9)$$

Using the following change of variables:

The governing Eqs. (1) to (8) reduce to non-dimensional form [64, 65]:

-For hybrid nanofluid

$$\frac{\partial u'_{nf}}{\partial x}+\frac{\partial v'_{nf}}{\partial y}=0 \quad (10)$$

$$u'_{nf}\frac{\partial u'_{nf}}{\partial x'}+v'_{nf}\frac{\partial u'_{nf}}{\partial y'}=-\frac{\partial p'}{\partial x'}+\frac{\mu_{nf}}{\rho_{nf}\nu_f}Pr\left(\frac{\partial^2 u'_{nf}}{\partial x'^2}+\frac{\partial^2 u'_{nf}}{\partial y'^2}\right)+\frac{\mu_{nf}}{\rho_{nf}\nu_f}\mathrm{Pr}Ha^2\sin(\gamma)\left(v'_{nf}\cos(\gamma)-u'_{nf}\sin(\gamma)\right) \quad (11)$$

$$u'_{nf}\frac{\partial v'_{nf}}{\partial x'}+v'_{nf}\frac{\partial v'_{nf}}{\partial y'}=-\frac{\partial p'}{\partial y'}+\frac{\mu_{nf}}{\rho_{nf}\nu_f}Pr\left(\frac{\partial^2 v'_{nf}}{\partial x'^2}+\frac{\partial^2 v'_{nf}}{\partial y'^2}\right)+\frac{(\rho\beta_T)_{nf}}{\rho_{nf}\beta_f}Ra\,Pr\,T'+\frac{\mu_{nf}}{\rho_{nf}\nu_f}\mathrm{Pr}Ha^2\cos(\gamma)\left(u'_{nf}\sin(\gamma)-v'_{nf}\sin(\gamma)\right) \quad (12)$$

$$u'_{nf}\frac{\partial T'_{nf}}{\partial x'}+v'_{nf}\frac{\partial T'_{nf}}{\partial y'}=\left(\frac{\alpha_{nf}}{\alpha_f}+\frac{4\alpha_{nf}Rd}{3\alpha_f}\right)\left(\frac{\partial^2 T'_{nf}}{\partial x'^2}+\frac{\partial^2 T'_{nf}}{\partial y'^2}\right)+\frac{\alpha_{nf}}{\alpha_f}\lambda T'_{nf} \quad (13)$$

-For porous layer

$$\frac{\partial u'_{po}}{\partial x'}+\frac{\partial v'_{po}}{\partial y'}=0 \quad (14)$$

$$u'_{po}\frac{\partial u'_{po}}{\partial x'}+v'_{po}\frac{\partial u'_{po}}{\partial y'}=-\frac{\partial p'}{\partial x'}+\frac{\mu_{nf}}{\rho_{nf}\nu_f}Pr\left(\frac{\partial^2 u'_{po}}{\partial x'^2}+\frac{\partial^2 u'_{po}}{\partial y'^2}\right)-\frac{Pr}{Da}u'_{po}+\frac{\mu_{nf}}{\rho_{nf}\nu_f}\mathrm{Pr}Ha^2\sin(\gamma)\left(v'_{nf}\cos(\gamma)-u'_{nf}\sin(\gamma)\right) \quad (15)$$

$$u'_{po}\frac{\partial v'_{po}}{\partial x'}+v'_{po}\frac{\partial v'_{po}}{\partial y'}=-\frac{\partial p'}{\partial y'}+\frac{\mu_{nf}}{\rho_{nf}\nu_f}Pr\left(\frac{\partial^2 v'_{po}}{\partial x'^2}+\frac{\partial^2 v'_{po}}{\partial y'^2}\right)+\frac{(\rho\beta_T)_{nf}}{\rho_{nf}\beta_f}Ra\,Pr\,T'-\frac{Pr}{Da}v'_{po}+\frac{\mu_{nf}}{\rho_{nf}\nu_f}\mathrm{Pr}Ha^2\cos(\gamma)\left(u'_{nf}\sin(\gamma)-v'_{nf}\sin(\gamma)\right) \quad (16)$$

$$x'=\frac{x}{W},y'=\frac{y}{W},u'=\frac{uW}{\alpha_f},v'=\frac{vW}{\alpha_f},T'=\frac{T-T_c}{T_h-T_c},p'=\frac{pW^2}{\rho_{nf}\alpha_f^2},Ra=\frac{g\beta_T(T_h-T_c)W^2}{\nu_f^2}\mathrm{Pr},\mathrm{Pr}=\frac{\nu_f}{\alpha_f},Da=\frac{K}{W^2}$$

$$\lambda=\frac{QW^2}{k},Rd=\frac{4\sigma_B{T_c}^3}{k\beta},Ha=B_oW\sqrt{\frac{\sigma_{nf}}{\rho_{nf}\nu_{nf}}}$$

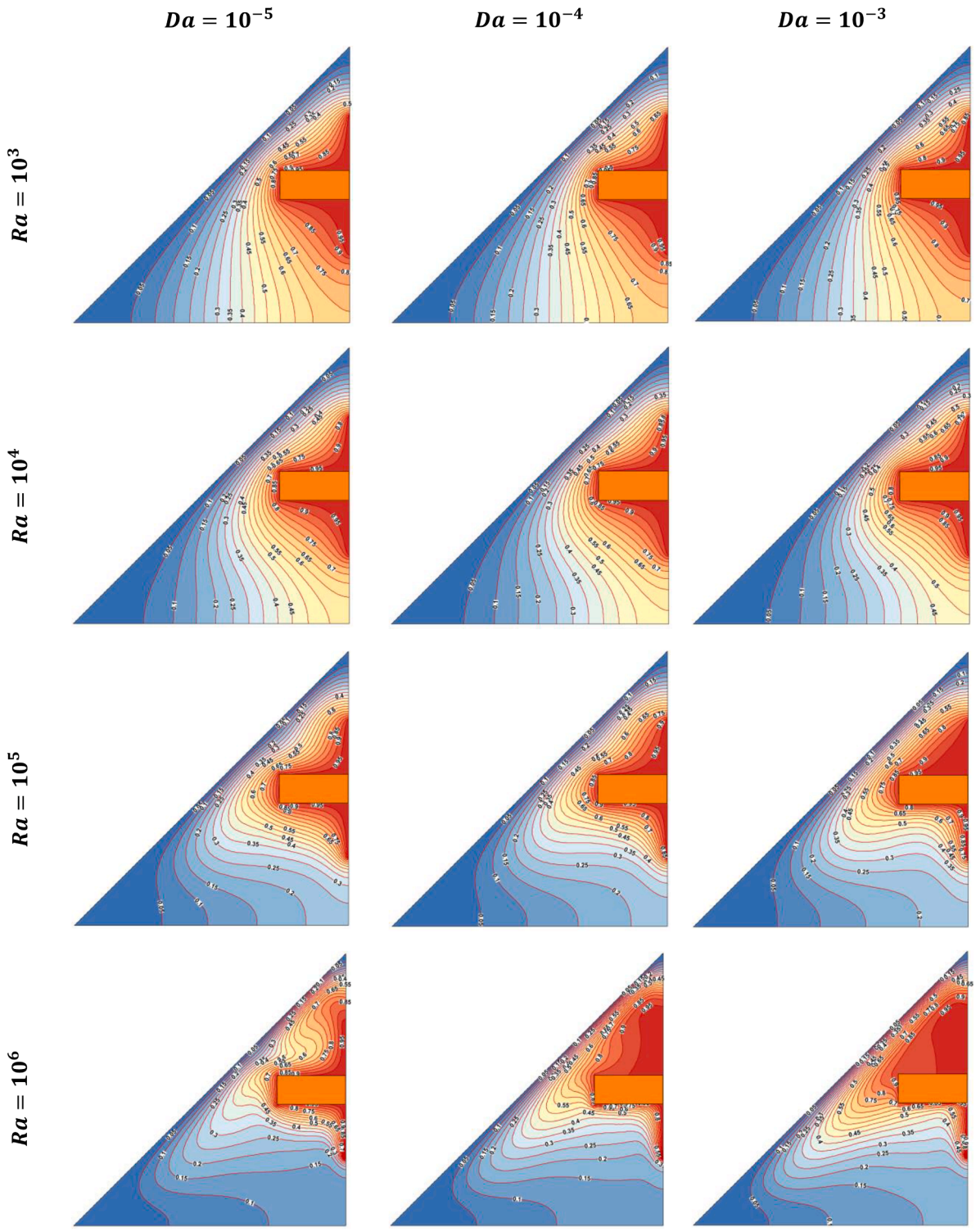

Fig. 8. Rayleigh number (Ra) effect on the isotherms for different Darcy numbers at $\varphi = 0.02$, $R = 0.4$ $Rd = 0, \lambda = 0$.

$$u'_{po}\frac{\partial T'_{po}}{\partial x'} + v'_{po}\frac{\partial T'_{po}}{\partial y'} = \left(\frac{\alpha_{nf}}{\alpha_f} + \frac{4\alpha_{nf}k_{eff}Rd}{3k_{nf}\alpha_f}\right)\left(\frac{\partial^2 T'_{po}}{\partial x'^2} + \frac{\partial^2 T'_{po}}{\partial y'^2}\right) + \frac{\alpha_{nf}}{\alpha_f}\frac{k_{eff}}{k_{nf}}\lambda T'_{po} \tag{17}$$

2.3. Boundary conditions and auxiliary equation

The dimensionless equations are solved by applying the following boundary conditions:

For the vertical surface acting as the heat source in the triangular enclosure at $x' = 0$, $y' = \left(\frac{W-s}{2}\ to\ \frac{W+s}{2}\right)$

$T' = 1$, $u' = 0$, $and v' = 0$

At the inclined cold walls of the triangular enclosure:

$T' = 0$, $u' = 0$, $and v' = 0$

At the insulation walls of the triangular enclosure:

$\frac{\partial T'}{\partial n} = 0$ ($where\ n\ is\ a\ normal\ direction$), $u' = 0$, $v' = 0$

The equation of the local and average *Nu* are presented as [60]:

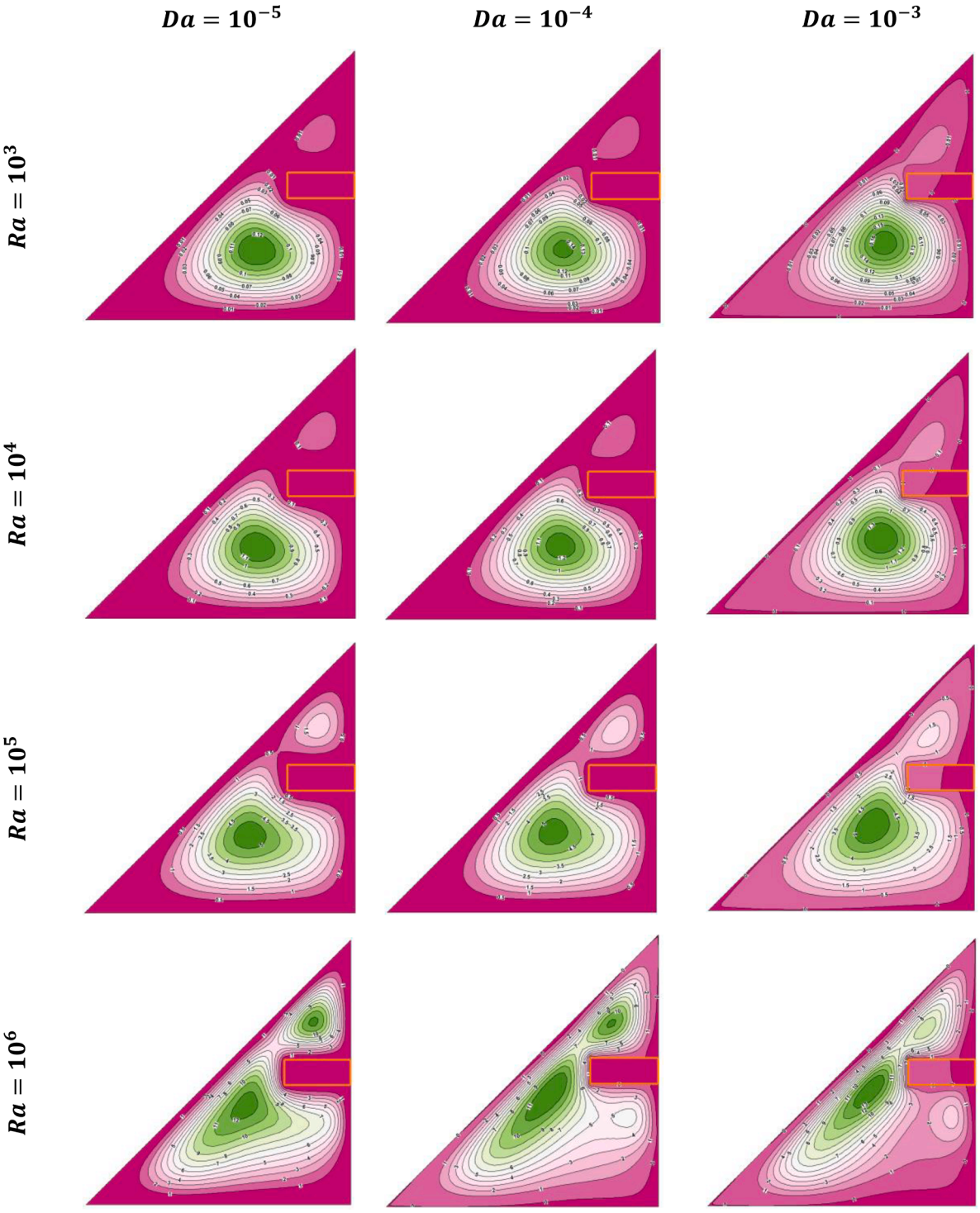

Fig. 9. Rayleigh number (Ra) effect on the streamlines for different Darcy numbers at $\varphi = 0.02$, AR = 0.4. Rd=0,$\lambda = 0$.

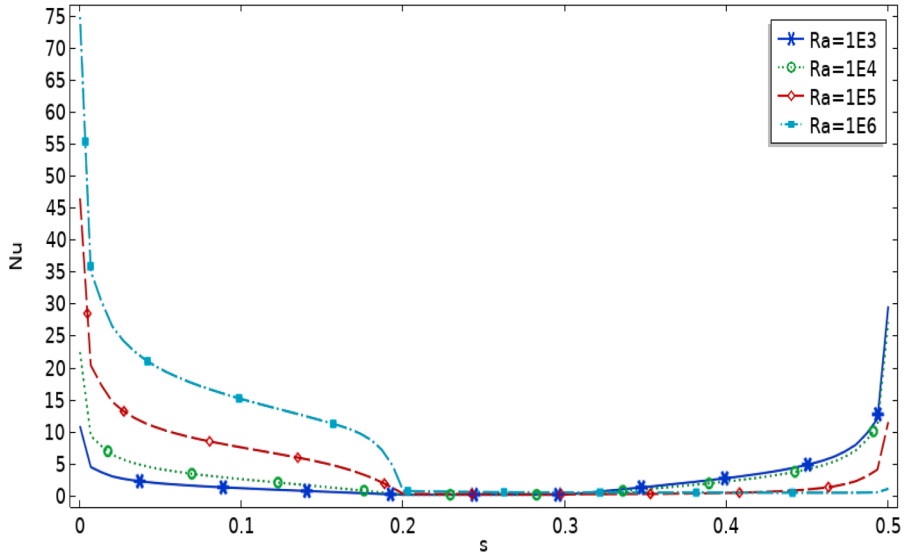

Fig. 10. Local Nusselt number variation along the vertical hot wall for various Ra at Da = 10^{-3}, φ = 0.02, and AR = 0.4 Rd = 0, λ = 0.

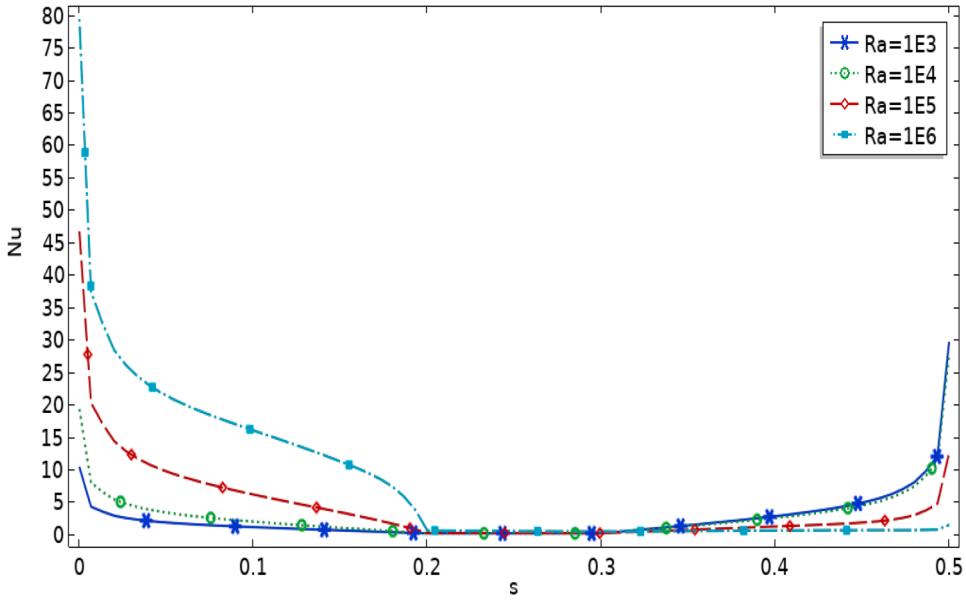

Fig. 11. Local Nusselt number variation along the vertical hot wall for various Ra at Da = 10^{-4}, φ = 0.02, and AR = 0.4. Rd = 0, λ = 0.

$$Nu_L = -\left(\frac{k_{nf}}{k_f} + \frac{4k_{nf}}{3k_f}Rd\right)\frac{\partial T'}{\partial y'} \tag{18}$$

$$Nu_{av} = \int_0^s Nu_L dy' \tag{19}$$

The equation of the stream function is [15]:

$$u' = \frac{\partial \psi}{\partial y'} \tag{20}$$

$$v' = -\frac{\partial \psi}{\partial x'} \tag{21}$$

$$\frac{\partial^2 \psi}{\partial x'^2} + \frac{\partial^2 \psi}{\partial y'^2} = \frac{\partial u'}{\partial y'} - \frac{\partial v'}{\partial x'} \tag{22}$$

The entropy generation associated to the fluid flow friction given by [66]:

$$s'''_{gen,\mu} = \frac{\mu_{nf}}{T_0}\left[2\left(\frac{\partial u}{\partial x}\right)^2 + 2\left(\frac{\partial v}{\partial y}\right)^2 + \left(\frac{\partial u}{\partial y} + \frac{\partial v}{\partial x}\right)^2\right] \tag{23}$$

where $T_0 = (T_H + T_C)/2$.

The entropy generation is associated to the heat transfer $s'''_{gen,h}$ given by [66]

$$s'''_{gen,h} = \frac{k_{nf}}{T_0^2}\left[\left(\frac{\partial T}{\partial x}\right)^2 + \left(\frac{\partial T}{\partial y}\right)^2\right] \tag{24}$$

In non-dimensional form of the total entropy generation (S'''_{gen}) becomes [66,67]:

$$S'''_{\text{gen}} = \frac{k_{nf}}{k_f}\left[\left(\frac{\partial \theta}{\partial X}\right)^2 + \left(\frac{\partial \theta}{\partial Y}\right)^2\right] + \chi\left[2\left(\frac{\partial U}{\partial X}\right)^2 + 2\left(\frac{\partial V}{\partial Y}\right)^2 + \left(\frac{\partial U}{\partial Y} + \frac{\partial V}{\partial X}\right)^2\right] \tag{25}$$

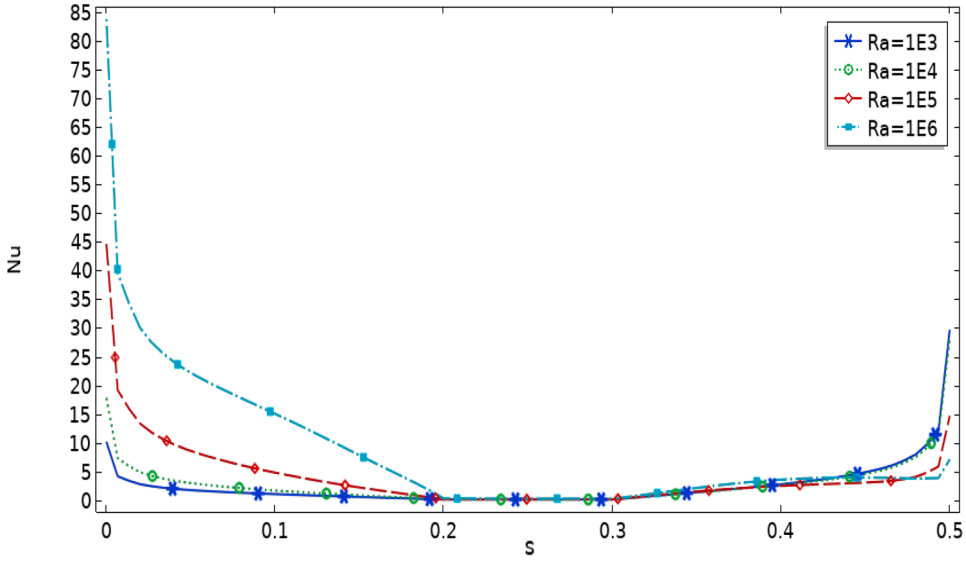

Fig. 12. Local Nusselt number variation along the vertical hot wall for various *Ra* at $Da = 10^{-5}$, φ = 0.02, and AR = 0.4. $Rd = 0$, λ = 0.

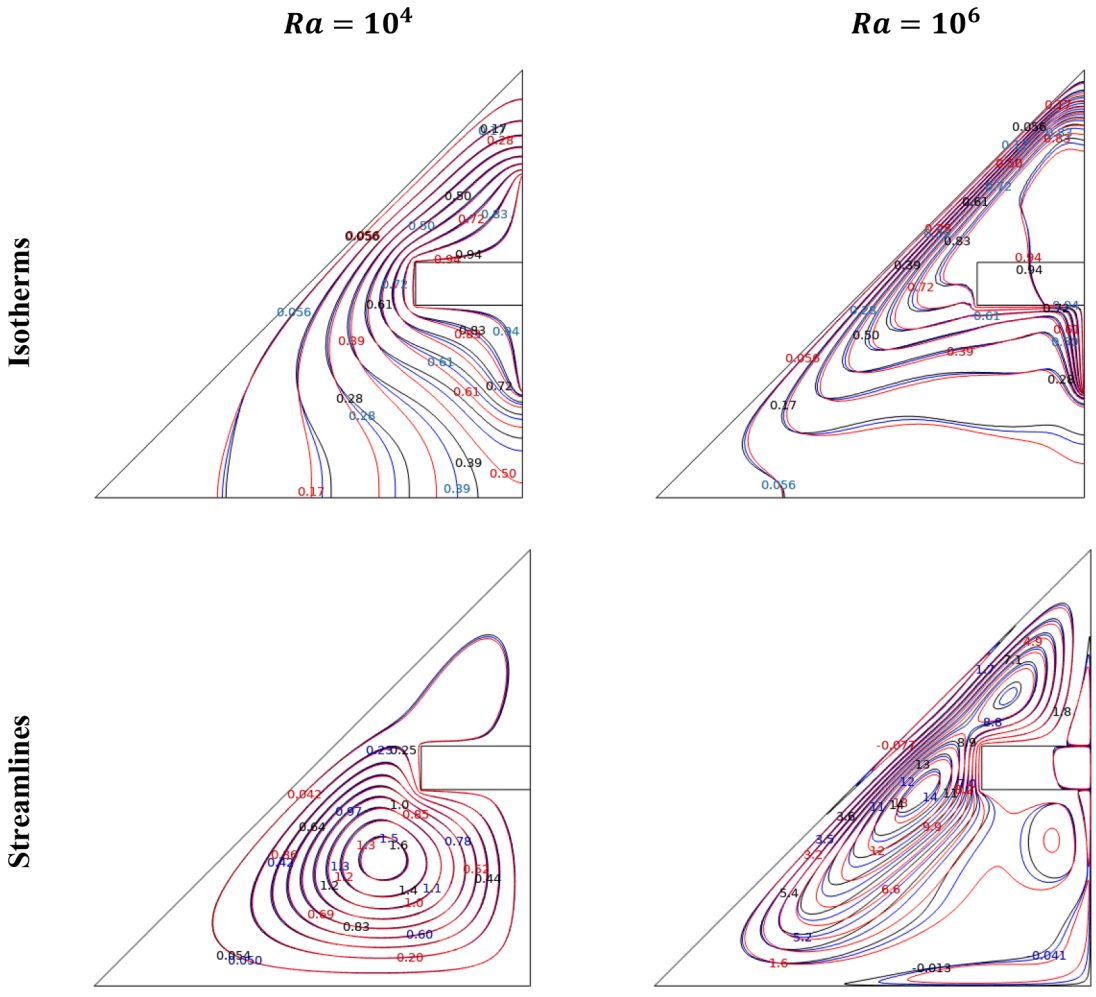

Fig. 13. The effect of nano volume concentration ratio on isotherms patterns and stream function (red for φ = 0.02, blue for φ = 0.01, black for φ = 0.0) at $Da = 10^{-3}$, $Rd = 0$, λ = 0, and $AR = 0.4$.

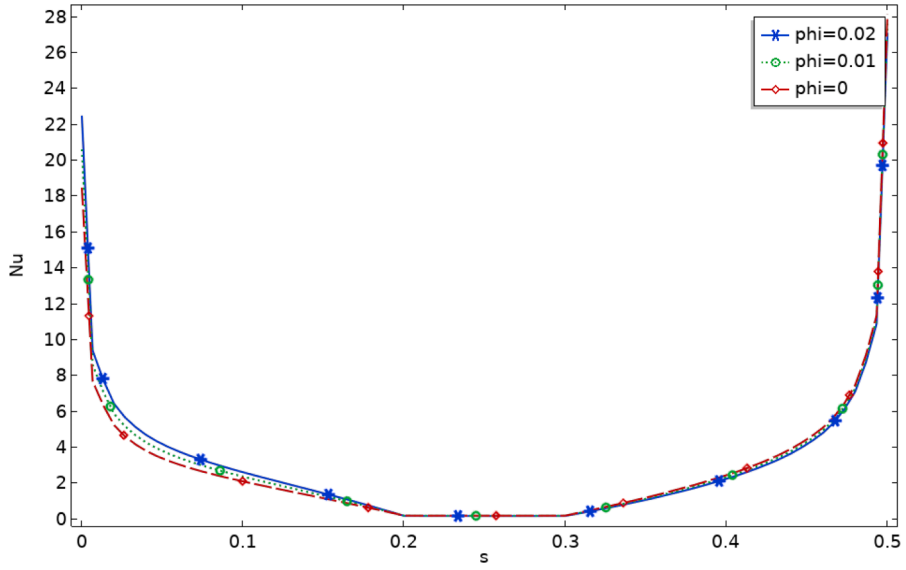

Fig. 14. Local Nusselt number variation along the vertical hot wall for various nano volume concentration ratio at $Da = 10^{-3}$, $Ra = 10^{3}$, $Rd = 0$, $\lambda = 0$ and AR = 0.4.

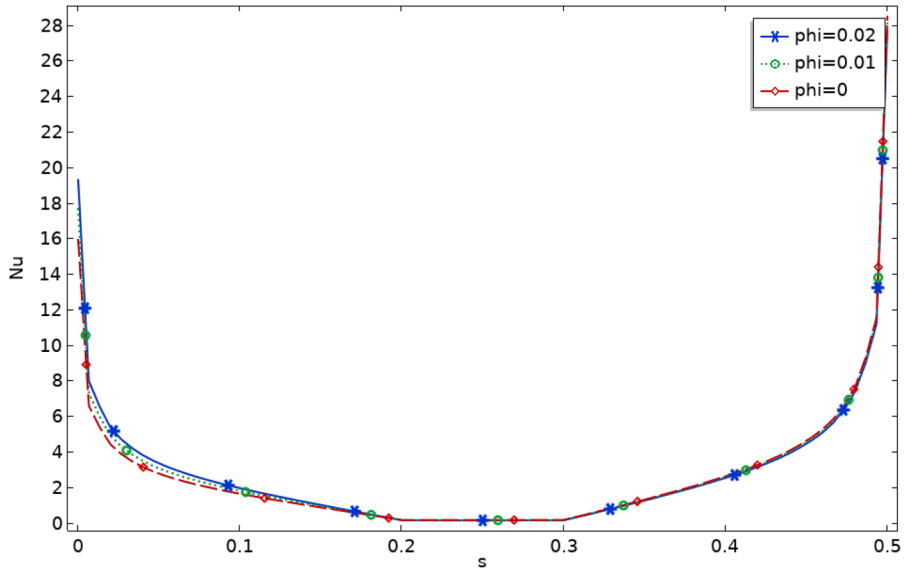

Fig. 15. Local Nusselt number variation along the vertical hot wall for various nano volume concentration ratio at $Da = 10^{-4}$, $Ra = 10^{3}$, $Rd = 0$, $\lambda = 0$, and AR = 0.4.

Where χ is irreversibility factor and given by [66]:

$$\chi = \frac{\mu_{nf} T_0}{k_f}\left(\frac{U_0}{T_H - T_c}\right) \tag{26}$$

The non-dimensional total entropy generation $\left(\dot{S}_{\text{gen}}\right)$ is given by:

$$\dot{S}_{gen} = \int S'''_{gen} dA \tag{27}$$

The Bejan number, Be, defined as the ratio between the entropy generation due to heat transfer by the total entropy generation, is expressed as [66]:

$$Be = \frac{S'''_{gen,h}}{S'''_{\text{gen}}} \tag{28}$$

2.4. Materials properties

The volumetric concentration φ of hybrid nanofluid (mixture of MgO and Ag nanoparticles suspended in carrier fluid water) is obtained as [68]:

$$\varphi = \varphi_{MgO} + \varphi_{Ag} \tag{29}$$

The thermodynamic properties of the base fluid and the two types of nanoparticles, *MgO* and *Ag*, are listed in Table 1. The effective thermophysical properties of the hybrid nanofluid are evaluated using standard empirical relations (the mixture rule), as listed in Table 2, where the subscripts *f* and *s* denote base fluid and solid nanoparticles (*MgO* and *Ag*), respectively. The porous fin is made of copper, and its effective thermal conductivity can be calculated using the equation from [68]:

$$k_{eff} = (1 - \varepsilon)\, k_p + \varepsilon\, k_{hnf} \tag{30}$$

Where ε is the porosity of the fin material, and $k_p$is the thermal conductivity of porous media solid material.

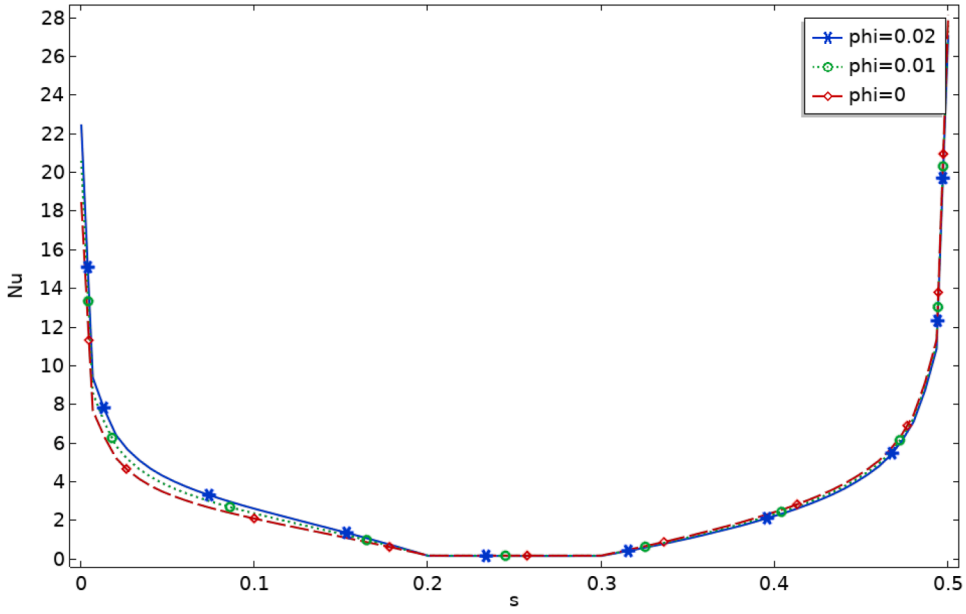

Fig. 16. Local Nusselt number variation along the vertical hot wall for various nano volume concentration ratio at $Da = 10^{-5}$, $Ra = 10^3$, $Rd = 0$, $\lambda = 0$, and AR = 0.4.

2.5. Solution procedure

In the current simulation, the Galerkin finite element method (FEM) has been employed to investigate the thermal behavior of a hybrid nanofluid undergoing natural convection around a porous fin in a triangular enclosure. The domain must be divided into a number of elements to be solved, and the numerical solutions are very sensitive to the number of these elements. To ensure accurate and reliable solutions, the non-dimensional variables (p', u', v', T') are solved iteratively until convergence is achieved. The convergence criterion used in this simulation is based on the relative change of the variables between successive iterations. The convergence criterion is defined as:

$$\left|\frac{\xi^{i+1} - \xi^{i}}{\xi^{i+1}}\right| \leq 10^{-5} \tag{37}$$

Given the steady-state nature of our study, we employed several methods to ensure the accuracy and reliability of our numerical solutions: Mesh Independence Study: We conducted a comprehensive mesh refinement analysis to ensure solution independence from spatial discretization. Convergence Criteria: Strict convergence criteria were applied to all solved variables. The simulations were considered converged when the residuals for continuity, momentum, and energy equations fell below 10^{-6}. This stringent criterion ensures the reliability of the steady-state solution. Iteration Independence: To verify the stability of our steady-state solution, we continued iterations beyond the point of convergence. No significant changes (less than 0.01 %) in key parameters were observed with additional iterations, confirming the robustness of our results. Validation with Benchmark Solutions: Our numerical model and methodology were validated against established benchmark solutions from the literature. Simulations were performed on a system with an Intel Core i7-10700K processor (3.8 GHz, 8 cores) and 32 GB DDR4 RAM, running Windows 10 Pro and COMSOL Multiphysics 6.2. The average CPU time per simulation was 10 min, with a range of 10 to 20 min depending on specific parameters. Total CPU time for all simulations was approximately 25 h. Variations in CPU time were primarily due to the complexity of flow patterns at higher Rayleigh numbers

2.6. Grid independence test

Grid independence testing is a crucial step in numerical simulations to ensure the accuracy and reliability of the results. It involves assessing the sensitivity of the solution to grid resolution, aiming to determine the optimal grid size that captures the essential features of the physical phenomena without excessive computational cost. A grid independence test was performed for the average Nusselt number and maximum stream function at $Da = 10^{-3}$, $Ra = 10^3$, $\varphi = 0.02$, and $AR = 0.4$. Table 3 presents eight grids tested in this study. It shows that the Nu_{av} value for grid 9 has a 0.059 % error, and the ψ_{max}has a 0.119 % error, demonstrating a mesh independent result. Therefore, grid 8 (12,299 elements) has been selected for this study in all cases, as shown in Fig. 2.

2.7. Model validation

The numerical results must be validated. To achieve this goal, two different types of comparisons were conducted. The first comparison, shown in Fig. 3, includes the validation of isotherms and streamlines between the present work and Alomari et al. [68] at $Ra = 10^6$ and $\varphi = 0.02$. The authors used $MgO - Ag - H_2O$ hybrid nanofluid in a trapezoidal enclosure under the effect of a magnetic field. A quantitative comparison was made by calculating the local Nusselt number distribution for the current study and comparing it with the previous study by Alomari et al. [68], as shown in Fig. 4. The maximum deviation in Nu was 1.2 % at $Ra = 10^6$.

The second comparison was with Basak et al. [64] results. Fig. 5 displays isotherms and streamlines from the present numerical code and Basak et al. [64] results for a square cavity filled with porous media at $Pr = 0.71$, $Ra = 10^6$, and $Da = 10^{-5}$. All these comparisons show very good agreement between the present and the previous calculations.

Fig. 6 shows a comparison of the local Nusselt number between the current study and the previous study by Basak et al. [64] at different values of the Darcy number. The streamline results were also compared with Chen and Cheng [70]'s experimental and numerical study, as shown in Fig. 7. It can be observed that the distribution of streamlines in a semicircular cavity shows close agreement between the current study and Chen and Cheng [70]'s solution.

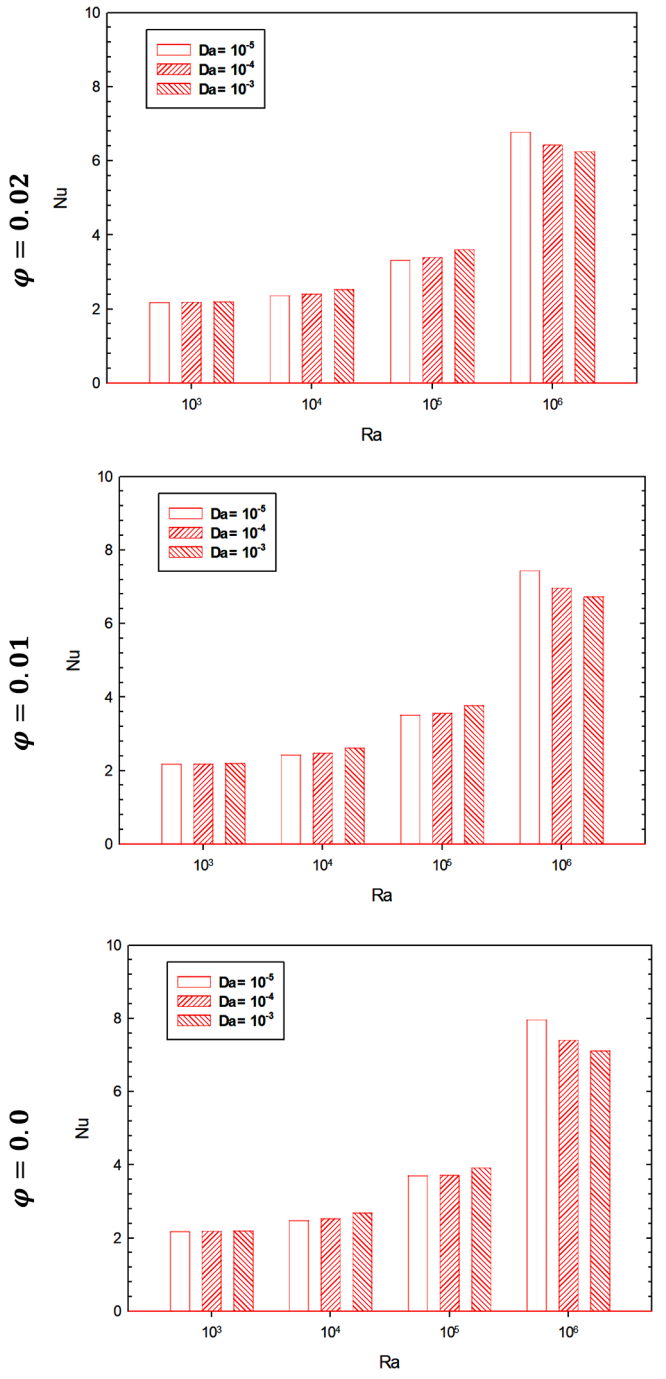

Fig. 17. Variation of average Nusselt number for different value of nano volume concentration ratio at AR = 0.4, $Rd = 0$, $and\lambda = 0$.

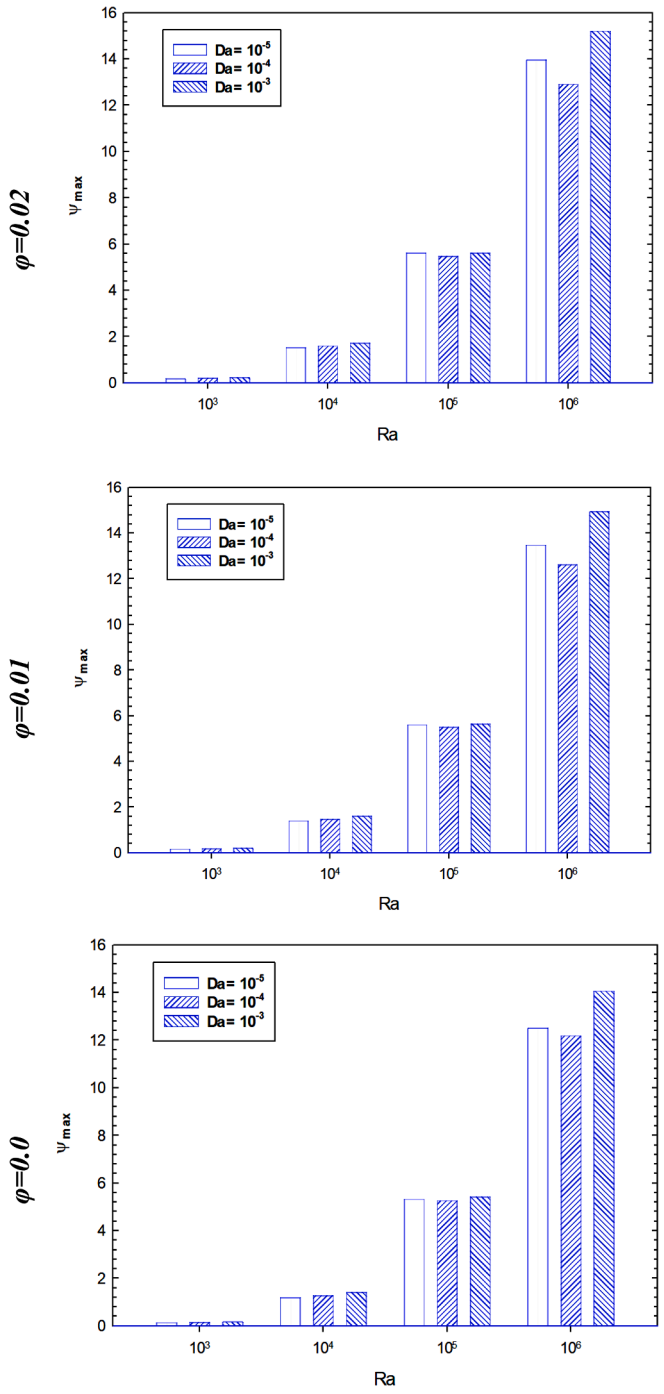

Fig. 18. Variation of maximum stream function for different value of nano volume concentration ratio at AR = 0.4, $Rd = 0$, $and\lambda = 0$.

3. Results

The results section presents the findings and outcomes of the thermal investigation of a hybrid nanofluid undergoing natural convection around a porous fin in a triangular enclosure. This section provides a comprehensive analysis of the obtained results, focusing on the temperature distribution, heat transfer enhancement, fluid flow patterns, and the impact of the porous fin. The results highlight the influence of various parameters on the thermal behavior of the system and offer valuable insights for optimizing heat transfer performance and thermal management in engineering applications. These parameters include Ra ($10^3 \leq Ra \leq 10^6$), Da ($10^{-5} \leq Da \leq 10^{-3}$), φ ($0 \leq \varphi \leq 0.02$), AR ($0.3 \leq AR \leq 0.6$).

3.1. Effect of Da and Ra

Fig. 8 illustrates the isotherms for different values of Da and Ra at $\varphi = 0.02$, $AR = 0.4$. For low values of $Ra(10^3 - 10^4)$, the buoyancy forces are weak. In this regime, the isotherms are nearly uniform around the porous fin and heated wall. The temperature difference across the fluid layer is minimal, and the heat transfer is relatively weak. For intermediate $Ra(10^5)$, the buoyancy forces become more significant, and natural convection starts to influence the heat transfer behavior. The isotherms around the porous fin exhibit variations. Heat transfer rates increase as Ra increases. For high $Ra(10^6)$, the isotherms exhibit significant variations, showing the formation of thermal plumes and convection cells

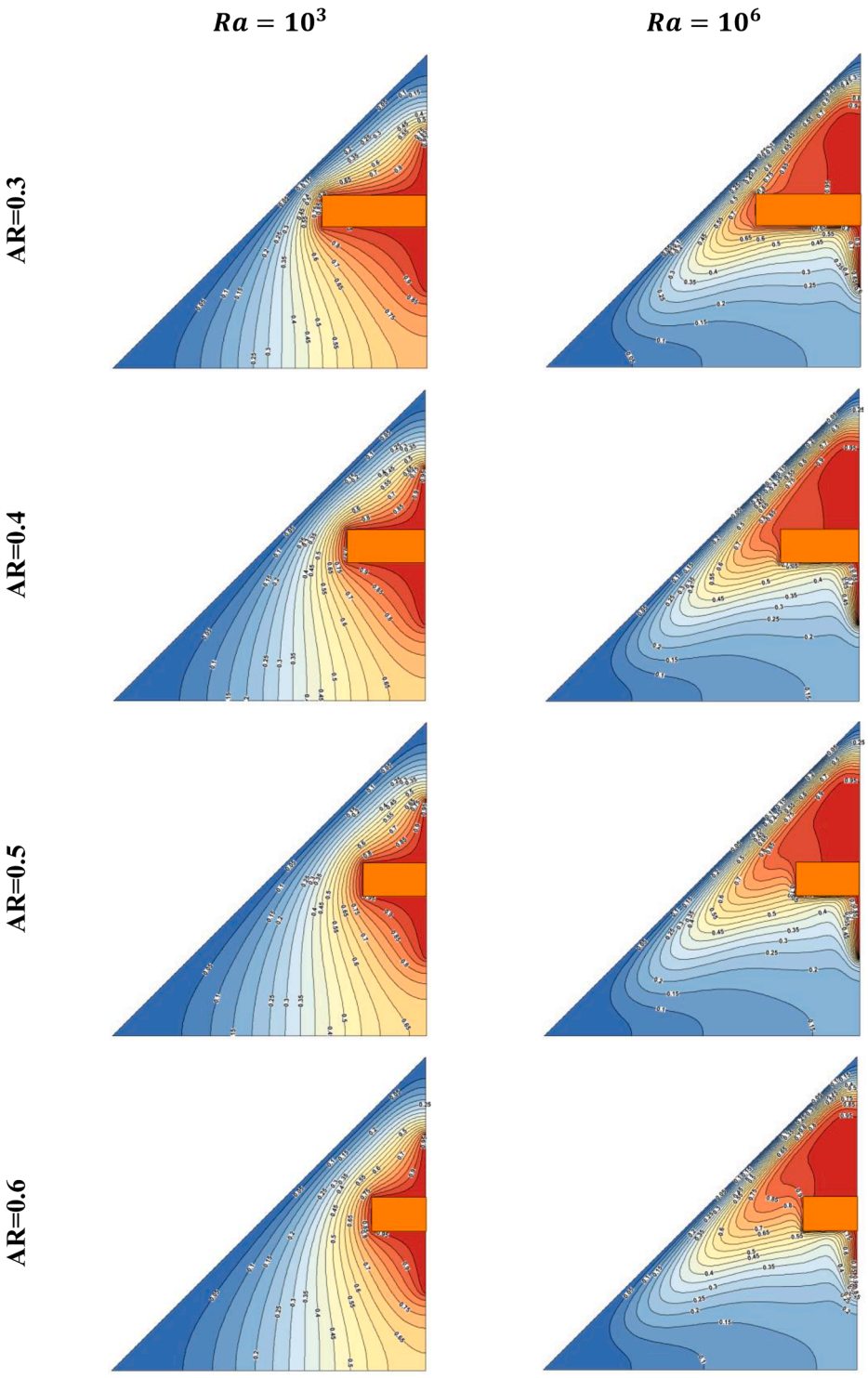

Fig. 19. Aspect ratio (AR) effect on the isotherms at φ=0.02, $Rd = 0$, $and\lambda = 0$.

within the fluid, as the buoyancy forces become dominant and natural convection becomes the primary mode of heat transfer. At low $Da(10^{-5})$, the isotherms near the porous fin are relatively uniform and parallel to the fin surface. The viscous forces dominate over inertial forces. For intermediate $Da(10^{-4})$, the isotherms show some deviations from uniformity. For high $Da(10^{-3})$, the inertial forces dominate over viscous forces. Heat transfer rates are significantly influenced by the inertial effects, and temperature gradients around the porous fin become more pronounced and non-uniform.

Fig. 9 shows the streamlines distribution through the triangular domain for different *Ra* and *Da*. As *Ra* increases, streamlines begin to deviate from their straight and parallel paths. The fluid flow becomes more complex with the formation of thermal plumes and convection cells. At $Ra = 10^3$, there is one circulation flow pattern in the center of the triangular domain. As *Ra* increases to 10^5, a second vortex appears above the porous fin near the upper corner of the enclosure. For high values of *Ra*, the streamlines show intricate patterns of fluid motion. For low values of *Da*, the streamlines around the porous fin are relatively straight and parallel, as the flow is smooth and laminar. The presence of the porous medium does not significantly alter the fluid flow behavior,

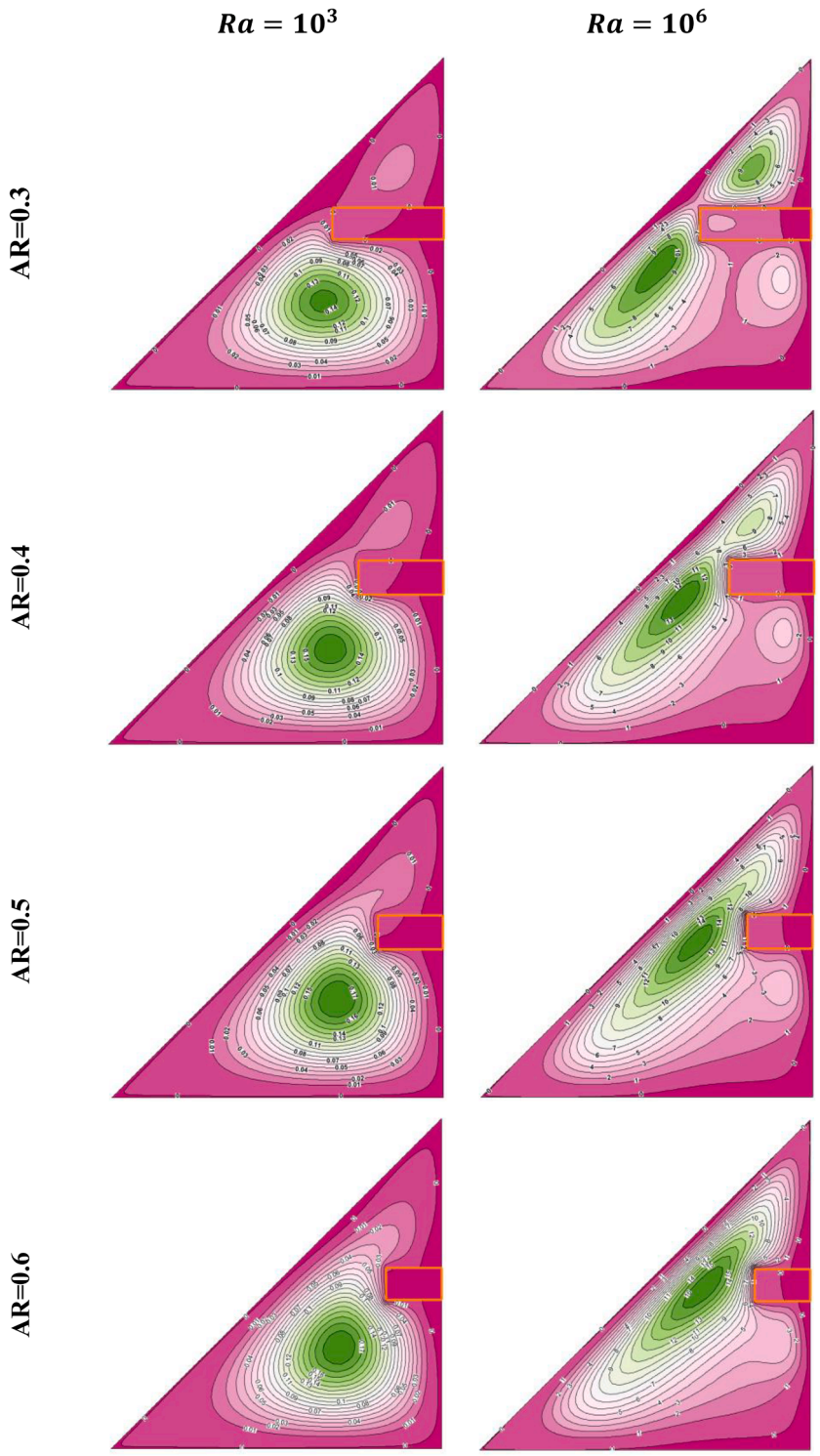

Fig. 20. Aspect ratio (AR) effect on the streamlines at φ=0.02, $Rd = 0$, $and\lambda = 0$.

and the streamlines remain relatively unaffected by the porous fin.

Figs. 10 **to** 12 demonstrate the variation of local *Nu* along the vertical heating wall at *Da* equal to 10^{-3},10^{-4},$and10^{-5}$, respectively. In the upper layer, the temperature difference is higher than in the lower layers because of the inclination of the cold wall, resulting in higher *Nu* values in the upper region which drop to lower values near the porous fin. As *Ra* increases, the local *Nu* variation along the vertical hot wall becomes more pronounced. The *Nu* typically increases from the bottom of the wall to the top due to the enhanced heat transfer caused by buoyancy-driven natural convection. The flow near the wall becomes more complex, and the heat transfer varies along the vertical direction, leading to non-uniform *Nu* distribution. For this range of *Da*, the viscous forces dominate over inertial forces, indicating slow and viscous-dominated fluid flow through the porous medium. In this regime, the flow near the vertical hot wall is relatively uniform, and the local Nusselt number variation along the wall is not significantly influenced by the presence of the porous fin. The heat transfer is primarily determined by conduction and convection near the wall, and the Nusselt number remains relatively

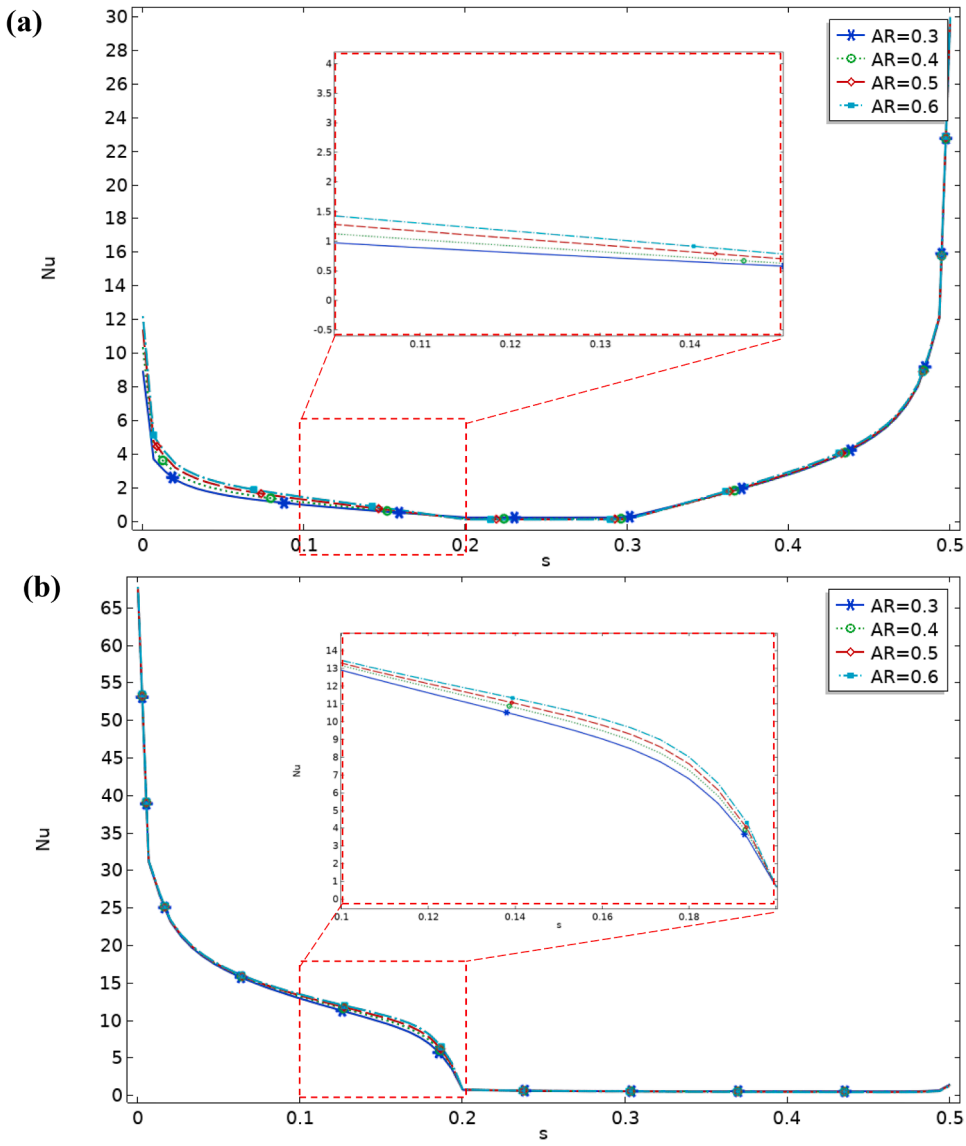

Fig. 21. Local Nusselt number variation along the vertical hot wall for various aspect ratio at $Da = 10^{-3}$, $\varphi = 0.02$, $Rd = 0$, $\lambda = 0$ (a)$Ra = 10^3$, and (b) $Ra = 10^6$.

constant along the vertical direction.

3.2. *Effect of nano volume concentration ratio*

Fig. 13 illustrates the effect of hybrid nano volume concentration on the isotherms and streamlines. Increasing the volume concentration ratio enhances the thermal conductivity and heat transfer capability of the nanofluid. As a result, the isotherms show reduced temperature gradients and a more uniform temperature distribution within the fluid. The presence of nanoparticles promotes heat dissipation, leading to lower temperatures near the heated wall. The nanoparticles alter the fluid viscosity and density, leading to changes in flow behavior. In the current study domain, the nano concentration does not affect streamlines for low values of *Ra*. At high *Ra*, buoyancy forces are much stronger than viscous forces, resulting in vigorous fluid motion and convection. The presence of nanoparticles in the hybrid nanofluid further enhances the fluid's buoyancy and density variations.

Figs. 14, 15, and 16 show the local Nusselt number distribution along the vertical heated wall for different values of Darcy number and nano volume concentration. Nano volume concentration significantly influences the local *Nu*. The presence of nanoparticles alters the thermal conductivity and viscosity of the fluid, improving the fluid's ability to carry heat away from the hot wall. As a result, the local *Nu* increases, indicating a higher rate of heat transfer near the surface compared to the base fluid without nanoparticles.

Fig. 17 shows the effect of *Ra* and *Da* on the average Nusselt number for different values of nano concentration. At low Rayleigh numbers (10^3,10^4,10^5), natural convection is not very significant, and the flow is primarily dominated by conduction. As the Darcy number (*Da*) increases, the flow through the porous medium becomes more efficient. The porous medium allows better flow of the fluid, reducing flow resistance, and enhancing heat transfer. Hence, the average Nusselt number increases with increasing *Da*. However, at high *Ra* (10^6), as the Darcy number (*Da*) increases, the fluid flow through the porous medium becomes more significant and less obstructed. This leads to the development of convective cells and thermal plumes within the porous medium, enhancing heat transfer. Consequently, the average Nusselt number increases with increasing *Da* up to a certain point. Increasing the nano volume concentration in the hybrid nanofluid also enhances the heat transfer capability. Nanoparticles have higher thermal conductivity than the base fluid, allowing them to carry heat more efficiently. As a result, the average Nusselt number increases with increasing nano volume concentration, indicating improved heat transfer performance.

Fig. 18 explains the effect of *Ra* and *Da* on the maximum stream

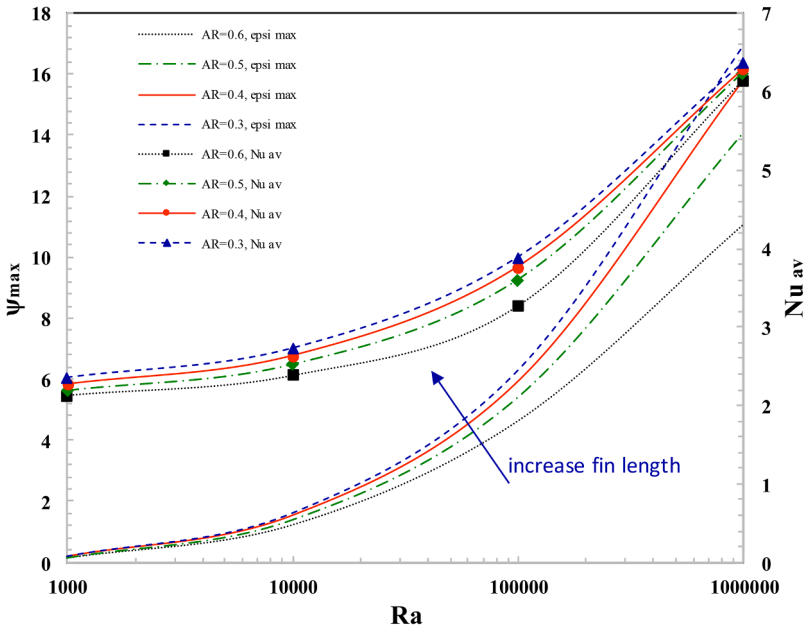

Fig. 22. Average Nusselt number and maximum stream function relation with *Ra* for different *AR*.

function (ψ_{max}). At 10^3 and 10^4 Rayleigh numbers, natural convection is not very significant, and the fluid flow is primarily driven by conduction. As the Darcy number (*Da*) increases, the fluid flow through the porous medium becomes more efficient. The porous medium allows better flow of the fluid, reducing flow resistance, and promoting fluid circulation. Consequently, ψ_{max} increases with increasing Da, indicating more significant fluid flow and enhanced circulation within the system. As the Darcy number (*Da*) increases at high *Ra*, the fluid flow through the porous medium becomes more efficient, leading to increased fluid circulation and stronger convection. Consequently, the maximum stream function initially increases with increasing *Da*, signifying enhanced fluid flow and convective heat transfer. Beyond a critical Darcy number, there might be an adverse effect on fluid flow due to increased fluid flow resistance caused by higher *Da* values. This can lead to a decrease in the maximum stream function as *Da* continues to increase beyond the critical value.

3.3. *Effect of aspect ratio*

Fig. 19 illustrates the effect of aspect ratio (*AR*) on isotherms. An increase in *AR* correlates with a decrease in the length of the porous fin. A longer porous fin (low *AR*) provides more surface area for heat transfer. As a result, the isotherms near the fin are likely to show more pronounced variations and gradients. The increased surface area allows for more contact between the fluid and the fin, facilitating heat exchange and leading to enhanced heat transfer rates. Consequently, the isotherms may exhibit steeper temperature gradients near the fin, indicating more efficient heat dissipation. With a shorter fin (higher *AR*), the heat transfer rates may be relatively lower near the fin. The isotherms might exhibit more gradual temperature variations, indicating a slower rate of heat dissipation. As *Ra* increases and natural convection becomes more influential, the impact of the fin length on the isotherms becomes more pronounced.

Fig. 20 shows the effect of *AR* on the streamlines. A longer porous fin creates more surface area and structure for fluid flow. As a result, the flow is forced to deviate from its original path, leading to changes in the streamlines. The fluid may split into multiple flow paths around the fin, resulting in the formation of thermal plumes, recirculation zones, and vortices. These flow structures are more pronounced with a longer fin. A shorter porous fin offers less obstruction to fluid flow. As a result, the flow path remains relatively undisturbed, and the streamlines are less affected by the presence of the fin. The fluid may experience minimal deflection around the fin, leading to simpler and more predictable flow patterns.

Fig. 21 shows the local *Nu* distributions along the vertical heated wall for different values of *AR*. At low Rayleigh numbers (Fig. 21**a**), natural convection effects are not very significant, and fluid flow is primarily driven by conduction. The length of the porous fin may have a relatively minor impact on the local Nusselt number distribution along the vertical wall. In this regime, the local Nusselt number distribution might be relatively uniform along the wall, indicating a relatively constant heat transfer rate. Longer fins might provide slightly enhanced heat transfer at the fin's base due to increased surface area, but the impact on the overall local *Nu* distribution might be limited. At high Rayleigh numbers (Fig. 21**b**), buoyancy forces dominate over viscous forces, leading to strong natural convection effects. Natural convection significantly influences the fluid flow and heat transfer patterns, making the fin length more influential on the local Nusselt number distribution along the vertical wall.

Fig. 22 illustrates the effect of *Ra* on the average Nusselt number and maximum stream function (ψ_{max}) for different *AR* values. Understanding this relationship can help optimize the design and performance of heat transfer systems involving porous fins under natural convection. For short fin lengths, heat transfer is relatively less efficient due to limited surface area for heat exchange. As a result, the average Nusselt number increases with increasing *Ra* from (2.1351) to (6.1547), but the increase is relatively modest compared to longer fins, which increase from (2.3573) to (6.3659). Short fins tend to have less impact on heat transfer enhancement compared to longer fins, especially at higher Ra where natural convection is more dominant. Regarding the Maximum Stream Function (ψ_{max}): Short fins have less effect on fluid flow obstruction, and the streamlines are less affected by the presence of the fin. Consequently, the maximum stream function increases with increasing *Ra*, but the increase is not as pronounced compared to longer fins. ψ_{max} increases from (0.14473) to (11.04) for shorter lengths, while for longer fins, it increases from (0.18961) to (16.922). The streamlines exhibit simpler patterns with minimal deflection around the short fin. Longer fins lead to higher average Nusselt numbers and maximum stream function values due to their ability to create complex flow patterns and provide more surface area for heat exchange.

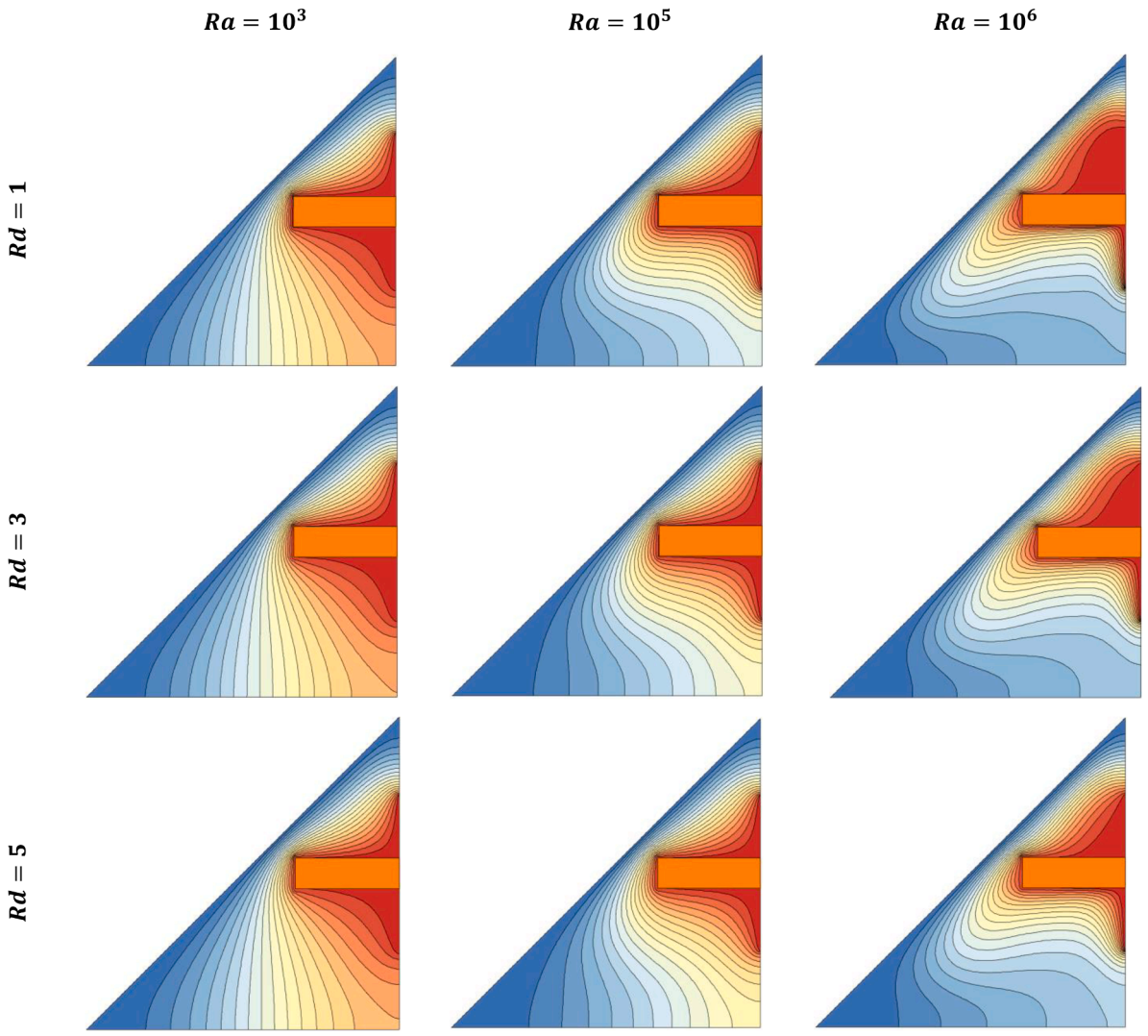

Fig. 23. Effect of radiation parameter (Rd) on isotherms. ($\lambda = 1$, $Da = 10^{-3}$, $\varphi = 0.02$, $AR = 0.3$).

3.4. Radiation parameters effect

The radiation parameter (*Rd*) represents the contribution of thermal radiation to the overall heat transfer process. Fig. 23 illustrates the influence of *Rd* on the isotherms and streamlines for a range of *Ra* and *Rd* values, with other parameters held constant. The isotherms appear to be less affected by the change in *Rd*. Furthermore, the isotherms show no noticeable change with variations in λ, as shown in Fig. 24**.** On the other hand, the average *Nu* values increase significantly with an increase in *Rd*, as can be seen in Table 4, while they are less influenced by changes in λ when $Rd = 1$.

3.5. Magnetohydrodynamic

Fig. 25 presents the influence of the Hartmann number and the inclination angle across a range of Rayleigh numbers on the average Nu number, with other parameters held constant. It is clear that the influence of MHD is only noticeable at high Ra numbers, where an increase in Ha number decreases the value of average Nu. On the other hand, increasing the inclination angle increases the value of average Nu at a constant Ha number. Furthermore, the influence of the Ha number and the inclination angle on the isotherms can be seen in Fig. 26. The isotherms are enhanced with an increase in the inclination angle. The same behavior is observed in Fig. 27 for the streamlines, where the strength of the streamlines increases with an increase in the inclination angle. The reason for this is the change in orientation of the MHD field and, according to the right-hand rule, the Lorentz force causes the streamlines to spread in different directions.

3.6. Entropy production

Fig. 28 shows the variation of total entropy generation (S_{total}) and Bejan number (*Be*) with Rayleigh number at different values of Darcy number. As *Ra* increases from 10^3 to 10^6, there's a significant increase in total entropy generation for all *Da* values. For $Da = 10^{-5}$, S_{total} increases from 7.2196 at $Ra = 10^3$ to 3074.6 at $Ra = 10^6$, a dramatic increase of about 42,500 %. This trend is consistent across all *Da* values, indicating that higher *Ra* leads to more irreversibilities in the system. At low *Ra* (10^3), the effect of *Da* on S_{total} is minimal. The difference between S_{total} for $Da = 10^{-5}$ and $Da = 10^{-3}$ is only about 0.48 %. As *Ra* increases, the impact of *Da* becomes more pronounced. At $Ra = 10^6$, S_{total} for $Da = 10^{-3}$ (4529) is about 47.3 % higher than for $Da = 10^{-5}$ (3074.6). Higher *Ra* causes an increase in total entropy generation due to increased irreversibilities resulting from increased fluid motion and heat transfer. A higher *Da* value indicates that the porous medium has higher permeability, facilitating fluid flow. This increased flow results in greater friction and mixing, leading to higher entropy generation, particularly at high *Ra* where convection dominates. As *Ra* increases from 10^3 to 10^6,

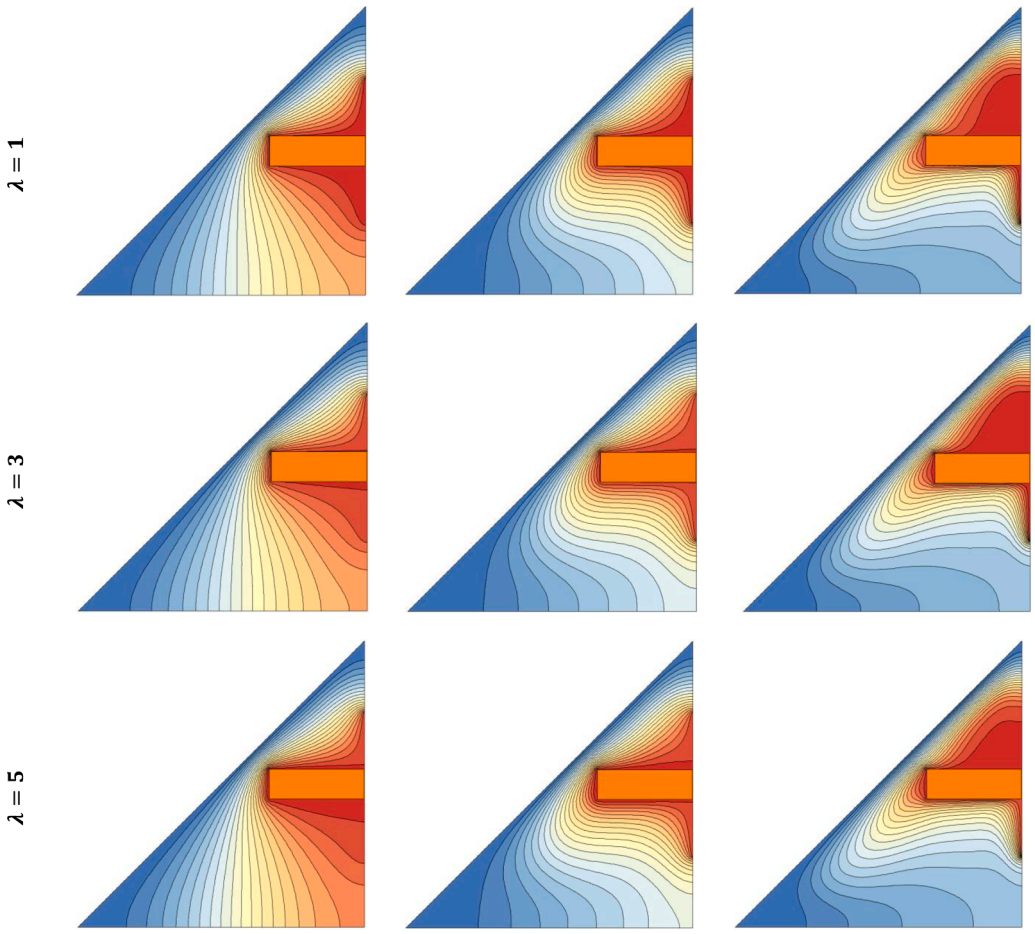

Fig. 24. Effect of heat generation parameter (λ) on isotherms. ($Rd = 1$, $Da = 10^{-3}$, $\varphi = 0.02$, $AR = 0.3$).

Table 4
Average Nusselt number results under the effect of radiation parameter at different value of *Ra*. ($Da = 10^{-3}$, $\varphi = 0.02$, $AR = 0.3$).

$Rd = 1$	$Ra = 10^3$	$Ra = 10^5$	$Ra = 10^6$	$\lambda = 1$	$Ra = 10^3$	$Ra = 10^5$	$Ra = 10^6$
$\lambda = 1$	$Nu_{avg=}$ 5.359	$Nu_{avg=}$7.560	$Nu_{avg=}$12.396	$Rd = 1$	$Nu_{avg=}$5.359	$Nu_{avg=}$7.560	$Nu_{avg=}$12.396
$\lambda = 2$	$Nu_{avg=}$8.622	$Nu_{avg=}$11.312	$Nu_{avg=}$17.205	$Rd = 2$	$Nu_{avg=}$5.027	$Nu_{avg=}$7.247	$Nu_{avg=}$12.002
$\lambda = 3$	$Nu_{avg=}$11.884	$Nu_{avg=}$14.849	$Nu_{avg=}$21.746	$Rd = 3$	$Nu_{avg=}$4.818	$Nu_{avg=}$7.064	$Nu_{avg=}$11.596
$\lambda = 4$	$Nu_{avg=}$15.145	$Nu_{avg=}$18.264	$Nu_{avg=}$26.194	$Rd = 4$	$Nu_{avg=}$4.650	$Nu_{avg=}$6.899	$Nu_{avg=}$11.484
$\lambda = 5$	$Nu_{avg=}$18.407	$Nu_{avg=}$21.608	$Nu_{avg=}$30.605	$Rd = 5$	$Nu_{avg=}$4.528	$Nu_{avg=}$6.750	$Nu_{avg=}$11.458

there's a significant decrease in the Bejan number for all *Da* values. For $Da = 10^{-3}$, *Be* decreases from 0.93814 at $Ra = 10^3$ to 0.020441 at $Ra = 10^6$, a reduction of about 97.8 %. This trend is consistent across all *Da* values, indicating that the relative importance of heat transfer irreversibilities decreases at higher *Ra*. At low *Ra*, heat transfer dominates, resulting in high *Be* values. As *Ra* increases, fluid friction becomes more significant, leading to a decrease in *Be*. The complex relationship between *Da* and *Be* at high *Ra* suggests an optimal permeability where heat transfer irreversibilities are maximized relative to fluid friction irreversibilities.

Fig. 29 presents contours of local entropy generation for various *Ra* and *Da*. The contours provide a spatial distribution of entropy generation within the enclosure, with S_{max} and S_{min} representing the highest and lowest local entropy generation rates, respectively. As *Ra* increases from 10^3 to 10^6, the contours show increasingly intense regions of high entropy generation. For $Da = 10^{-5}$, the peak intensity in the contours increases from 1886.5 at $Ra = 10^3$ to 1.27E+05 at $Ra = 10^6$, indicating a dramatic intensification of local irreversibilities. The contour patterns show a transition from more uniform distributions at low *Ra* to highly localized hot spots of entropy generation at high *Ra*. At $Ra = 10^3$, the contours for different *Da* values are similar, with only slight variations in peak intensity (1886.5 for $Da = 10^{-5}$ vs. 1874.6 for $Da = 10^{-3}$). As *Ra* increases, the contours for higher *Da* values show more intense localized regions of entropy generation. At $Ra = 10^6$, the peak intensity for $Da = 10^{-3}$ (2.19E+05) is significantly higher than for $Da = 10^{-5}$ (1.27E+05).

4. Conclusions

This study presents novel insights into the radiation influence on free convection in a cavity filled with a hybrid nanofluid and attached to a porous fin under the combined effects of magnetohydrodynamics and thermal radiation. The most important results are concluded as:

1. Flow and heat transfer characteristics: The streamlines and isotherms are enhanced with an increase in *Ra*. Furthermore, the average Nu value also increases with increasing *Ra*. The average Nu value increases with increasing volume concentration and radiation

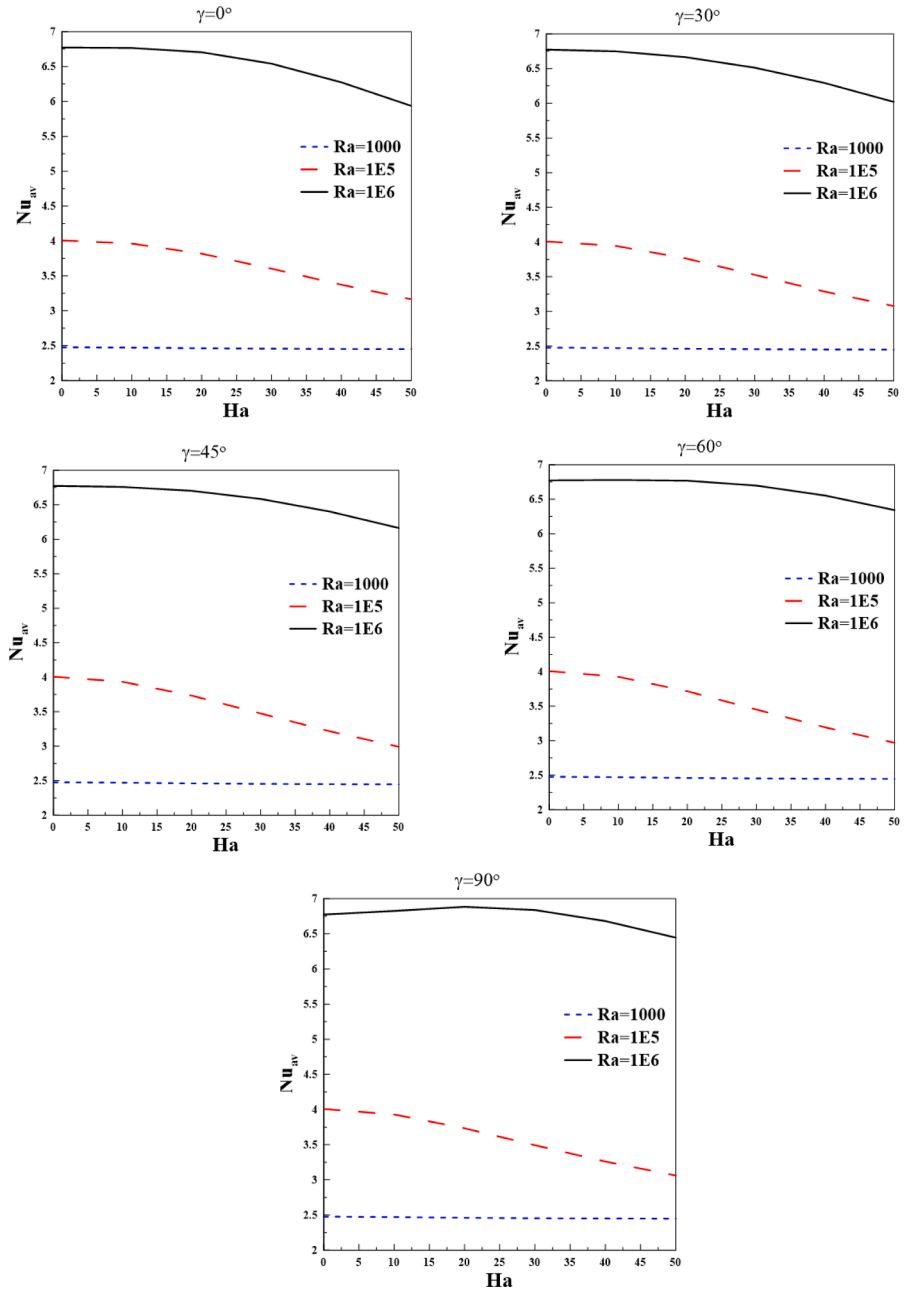

Fig. 25. Average Nusselt number relation with Ha for different γ and *Ra* at $Da = 10^{-3}$,φ = 0.02, and $AR = 0.3$.

parameter. However, the increase in average Nu due to the Rd number is greater than the effect of ϕ.

2. Critical Darcy number discovery: The influence of the *Da* number is only noticeable at high *Ra* numbers, where a critical *Da* value was discovered beyond which increasing *Da* decreases the average Nu value at high *Ra* numbers and vice versa for low *Ra* numbers.
3. Contrasting effects of radiation parameters: The radiation parameter (*Rd*) increases the average Nu value and also enhances the streamlines. In contrast, increasing the radiation parameter (λ) [leads to a drop in average Nu and decreases the strength of streamlines.
4. MHD and inclination angle effects: Increasing *Ha* decreases the strength of the streamlines and hence reduces heat transfer. However, increasing the inclination angle increases heat transfer and streamline strength.
5. Entropy generation analysis: Our comprehensive entropy generation study revealed complex interactions between system parameters and irreversibilities. Entropy generation generally increases with *Ra*, but the relative contributions of heat transfer and fluid friction to total entropy generation vary significantly with other parameters.
6. Future work: This study opens up several avenues for future research. Experimental validation of our numerical results could provide further insights and confirm the observed phenomena. Extending the analysis to transient conditions would offer valuable understanding of system behavior during startup or under fluctuating conditions. Advanced nanofluid models incorporating Brownian motion and thermophoresis could refine our understanding of nanoparticle behavior. Formal optimization studies could determine ideal parameter combinations for specific applications.

Funding

This research received no external funding.

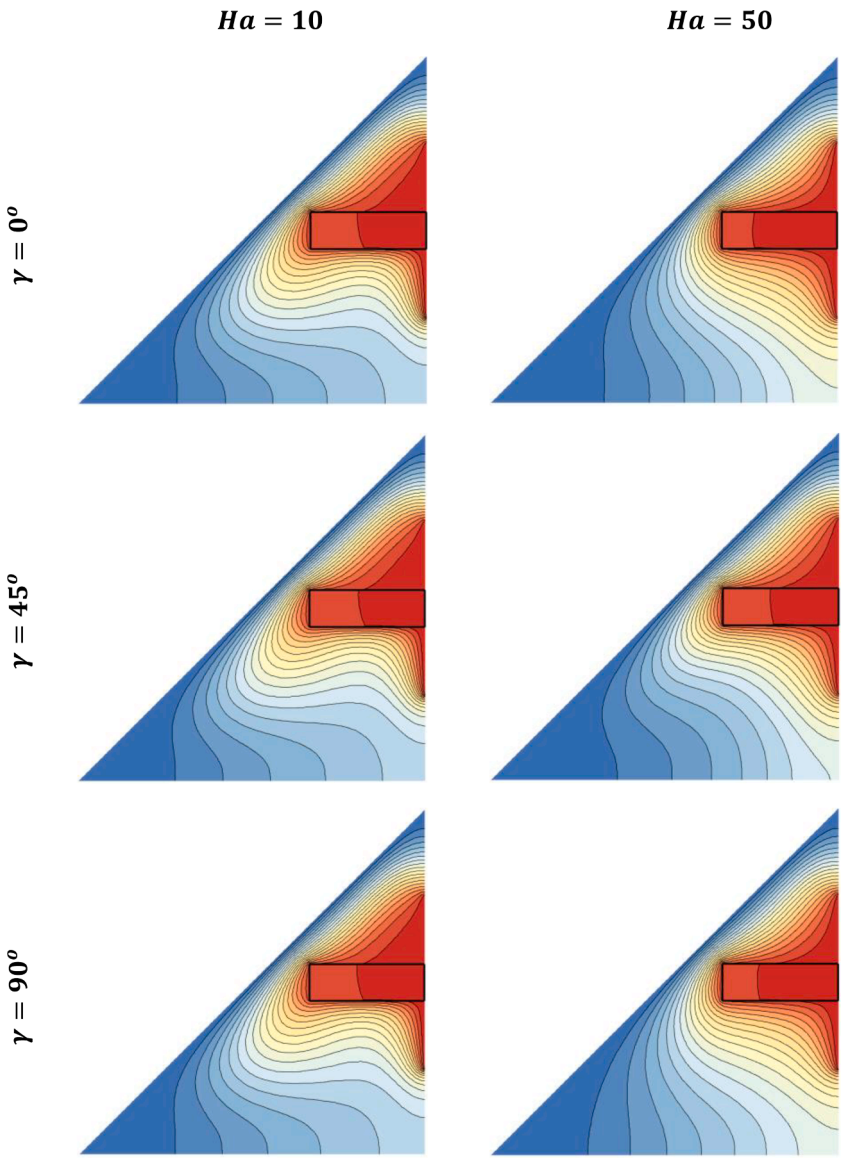

Fig. 26. Isotherm contour with varying γ and *Ha* at $Ra = 10^5$, $Da = 10^{-3}$, φ = 0.02, and $AR = 0.3$.

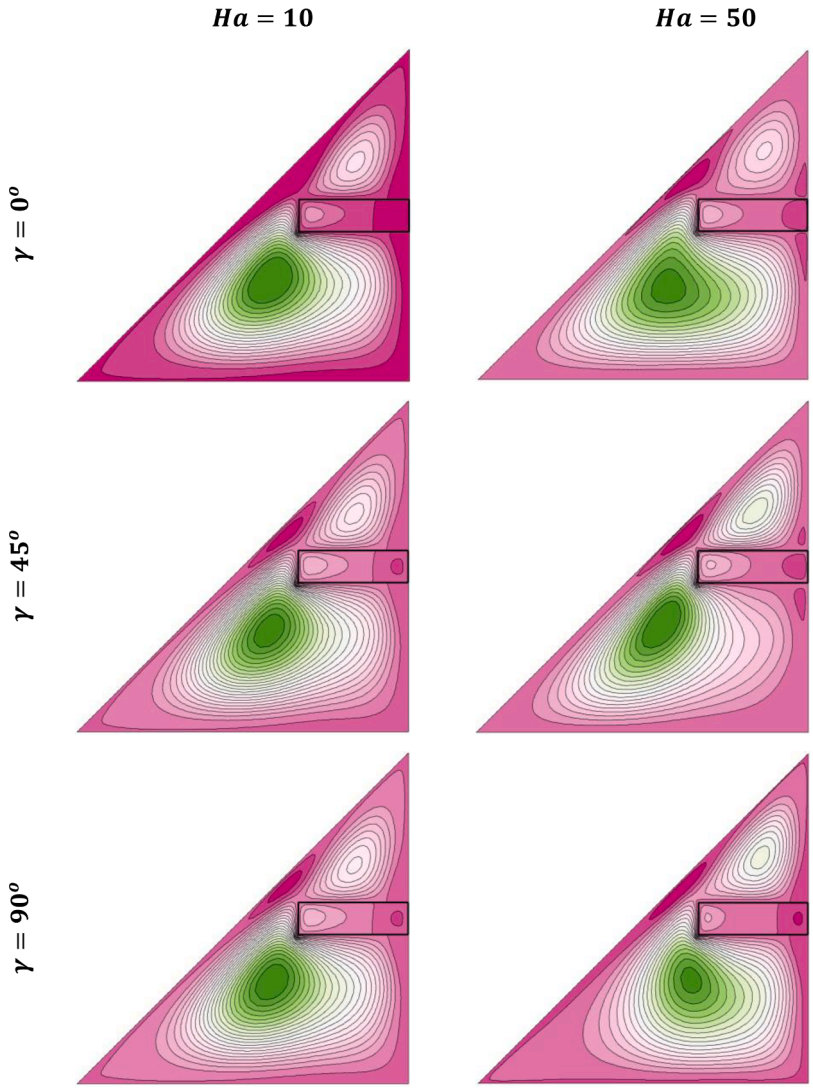

Fig. 27. Streamlines contour with varying γ and *Ha* at $Ra = 10^5$, $Da = 10^{-3}$, φ = 0.02, and $AR = 0.3$.

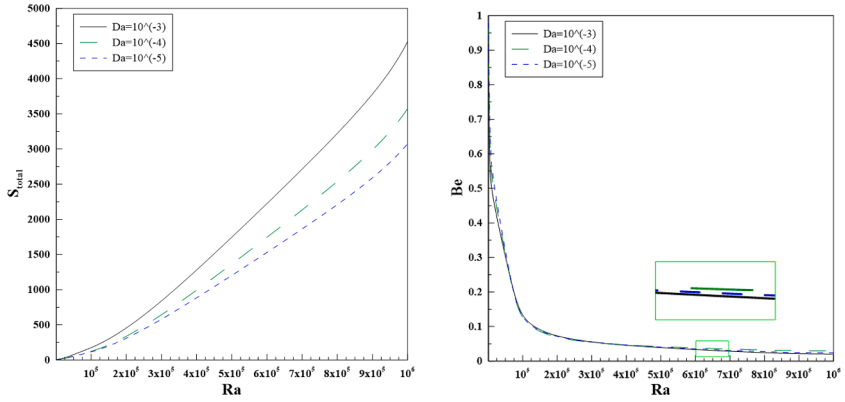

Fig. 28. Total entropy generation and Bejan number variation with Ra at different value of Da (for γ = 0, *Ha* = 10, φ = 0.01, and AR = 0.4).

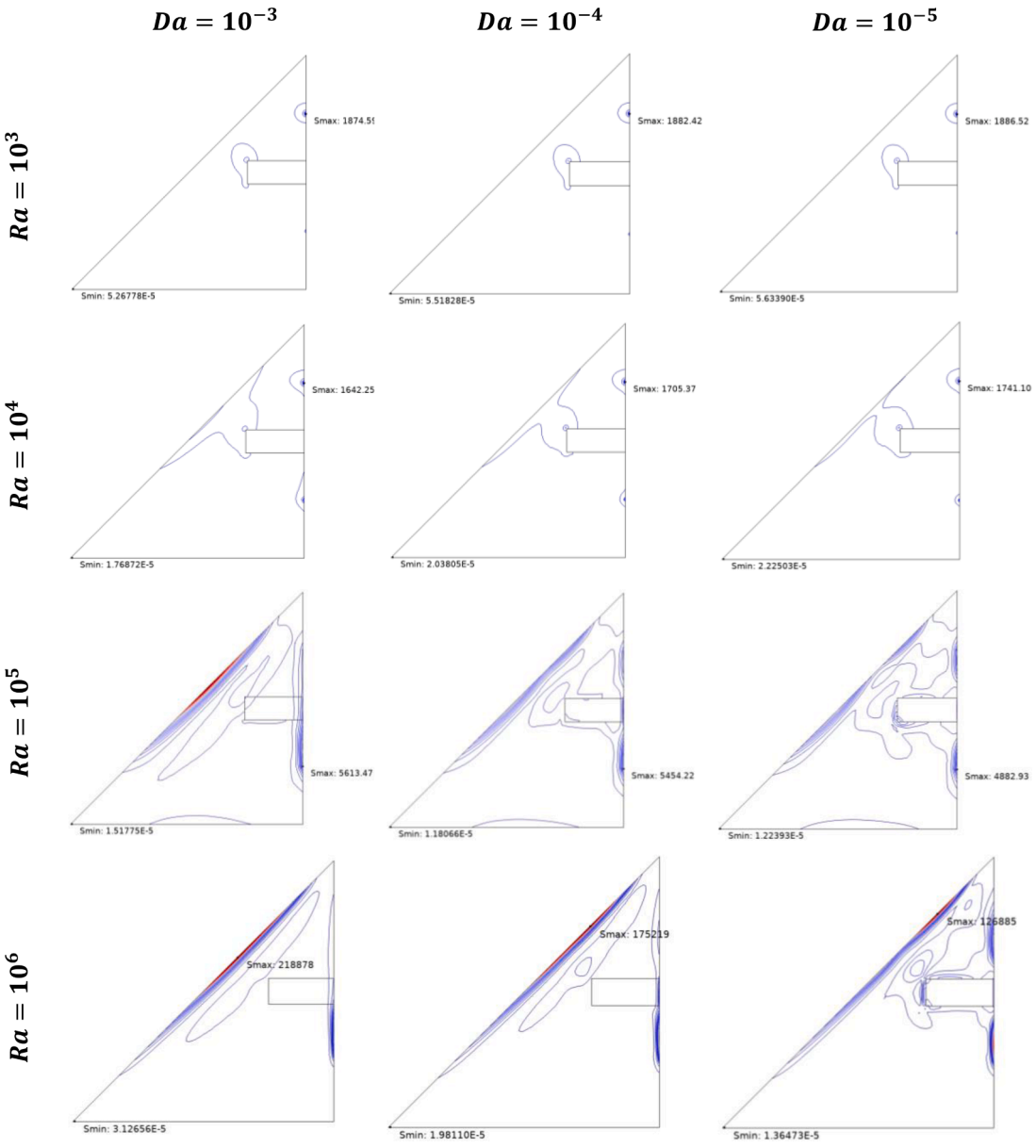

Fig. 29. *Total entropy generation contour variation with Ra at different value of Da (for* $\gamma = 0$, $Ha = 10$, $\varphi =$ ***0.01, AR = 0.4)***.

CRediT authorship contribution statement

Ahmed M. Hassan: Writing – original draft, Validation. **Mohammed Azeez Alomari:** Writing – review & editing, Resources. **Qusay H. Al-Salami:** Methodology, Formal analysis. **Farah Q.A. Alyousuf:** Writing – review & editing. **Faris Alqurashi:** Investigation. **Mujtaba A. Flayyih:** Project administration.

Declaration of competing interest

The authors declare that they have no known competing financial interests or personal relationships that could have appeared to influence the work reported in this paper.

Data availability

Data will be made available on request.

Acknowledgments

None.

References

[1] P.H.S. Carvalho, M.J.S. de Lemos, Double-diffusive laminar free convection in a porous cavity simulated with the two-energy equation model, Int. Commun. Heat Mass Transf. 82 (2017) 89–96, https://doi.org/10.1016/j.icheatmasstransfer.2017.02.005.

[2] H. Singh, P.C. Eames, Correlations for natural convective heat exchange in CPC solar collector cavities determined from experimental measurements, Sol. Energy 86 (9) (2012) 2443–2457, https://doi.org/10.1016/j.solener.2012.05.014.

[3] H. Bhowmik, K.W. Tou, Experimental study of transient natural convection heat transfer from simulated electronic chips, Exp. Therm. Fluid. Sci. 29 (4) (2005) 485–492, https://doi.org/10.1016/j.expthermflusci.2004.06.003.

[4] Y. Li, M. Firouzi, A. Karimipour, M. Afrand, Effect of an inclined partition with constant thermal conductivity on natural convection and entropy generation of a nanofluid under magnetic field inside an inclined enclosure: applicable for electronic cooling, Adv. Powder Technol. 31 (2) (2020) 645–657, https://doi.org/10.1016/j.apt.2019.11.020.

[5] A. Purusothaman, Investigation of natural convection heat transfer performance of the QFN-PCB electronic module by using nanofluid for power electronics cooling

applications, Adv. Powder Technol. 29 (4) (2018) 996–1004, https://doi.org/10.1016/j.apt.2018.01.018.
[6] A. Purusothaman, A. Baïri, K. Murugesan, Thermal state of electronic assemblies equipped with an array of heaters and coolers (HACs) subjected to natural convection, Therm. Sci. Eng. Prog. 11 (2019) 317–324, https://doi.org/10.1016/j.tsep.2019.04.008.
[7] E. Abbasi-Shavazi, J.F. Torres, G. Hughes, J. Pye, Experimental correlation of natural convection losses from a scale-model solar cavity receiver with non-isothermal surface temperature distribution, Sol. Energy 198 (2020) 355–375, https://doi.org/10.1016/j.solener.2020.01.023.
[8] V.R. Mugi, V.P. Chandramohan, Energy and exergy analysis of forced and natural convection indirect solar dryers: estimation of exergy inflow, outflow, losses, exergy efficiencies and sustainability indicators from drying experiments, J. Clean. Prod. 282 (2021). 10.1016/j.jclepro.2020.124421.
[9] Y. Abbassi, S. Asgarian, E. Ghahremani, M. Abbasi, Investigation of natural convection in miniature neutron source reactor of Isfahan by applying the porous media approach, Nucl. Eng. Des. 309 (2016) 213–223, https://doi.org/10.1016/j.nucengdes.2016.09.019.
[10] R. Freile, M. Tano, P. Balestra, S. Schunert, M. Kimber, Improved natural convection heat transfer correlations for reactor cavity cooling systems of high-temperature gas-cooled reactors: from computational fluid dynamics to Pronghorn, Ann. Nucl. Energy 163 (2021) 108547, https://doi.org/10.1016/j.anucene.2021.108547.
[11] M. Hashemi-Tilehnoee, E.P. del Barrio, S.M. Seyyedi, Magneto-turbulent natural convection and entropy generation analyses in liquid sodium-filled cavity partially heated and cooled from sidewalls with circular blocks, Int. Commun. Heat Mass Transf. 134 (2022) 106053, https://doi.org/10.1016/j.icheatmasstransfer.2022.106053.
[12] F.L. Rashid, A.K. Hussein, E.H. Malekshah, A. Abderrahmane, K. Guedri, O. Younis, Review of heat transfer analysis in different cavity geometries with and without nanofluids, Nanomaterials 12 (14) (2022) 2481.
[13] C. Qi, X. Cui, Y. Liu, Z. Yang, C. Huang, Natural convection heat transfer of liquid metal gallium nanofluids in a rectangular enclosure, Heat Transf.—Asian Res. 46 (1) (2017) 1–17.
[14] K.K. Al-Chlaihawi, H.H. Alaydamee, A.E. Faisal, K. Al-Farhany, M.A. Alomari, Newtonian and non-Newtonian nanofluids with entropy generation in conjugate natural convection of hybrid nanofluid-porous enclosures: a review, Heat Transf. 51 (2) (2022) 1725–1745.
[15] R.A. Hussein, A.M. Hassan, and R.H.J.N.H.T. Hameed, Part B: fundamentals, Mixed convection heat transfer in a partial porous layered split lid-driven wavy wall cavity with Cu–H2O nanofluid, 1–27 (2024).
[16] T. Tayebi, A.J. Chamkha, Natural convection enhancement in an eccentric horizontal cylindrical annulus using hybrid nanofluids, Numer. Heat Transf. A: Appl. 71 (11) (2017) 1159–1173.
[17] P. Dadheech, P. Agrawal, F. Mebarek-Oudina, N. Abu-Hamdeh, A. Sharma, Comparative heat transfer analysis of MoS2/C2H6O2 and SiO2-MoS2/C2H6O2 nanofluids with natural convection and inclined magnetic field, J. Nanofluids 9 (3) (2020) 161–167.
[18] S. Giwa, M. Sharifpur, M. Ahmadi, J. Meyer, A review of magnetic field influence on natural convection heat transfer performance of nanofluids in square cavities, J. Therm. Anal. Calorim. 145 (2021) 2581–2623.
[19] A.I. Alsabery, et al., Convection heat transfer in enclosures with inner bodies: a review on single and two-phase nanofluid models, Renew. Sustain. Energy Rev. 183 (2023) 113424, https://doi.org/10.1016/j.rser.2023.113424.
[20] S.S. Samantaray, et al., Recent advances on entropy analysis of composite nanofluids-A critical review, Results. Eng. 22 (2024) 101980, https://doi.org/10.1016/j.rineng.2024.101980.
[21] R.H. Hameed, A.M. Hassan, R.A. Hussein, A. Oliwie, and N.H.J.T.E.P.J.P. Hamza, CFD analysis of mixed convection and entropy generation in vented curved cavity under the radiation effects. 139 (8), 756 (2024).
[22] K. Guedri, et al., Investigation of free convection in a wavy trapezoidal porous cavity with MWCNT- Fe3O4/Water hybrid nanofluid under MHD effects: galerkin finite element analysis, Case Stud. Therm. Eng. 56 (2024) 104243, https://doi.org/10.1016/j.csite.2024.104243.
[23] S.A.M. Mehryan, F.M. Kashkooli, M. Ghalambaz, A.J. Chamkha, Free convection of hybrid Al2O3-Cu water nanofluid in a differentially heated porous cavity, Adv. Powder Technol. 28 (9) (2017) 2295–2305, https://doi.org/10.1016/j.apt.2017.06.011.
[24] M.N. Huda, M.S. Alam, S.M.C. Hossain, Optimization and sensitivity analysis of hydromagnetic convective heat transfer in a square cavity filled with a porous medium saturated by Ag-MgO/water hybrid nanofluid using response surface methodology, Int. J. Thermofluids 22 (2024) 100626, https://doi.org/10.1016/j.ijft.2024.100626.
[25] M. Mahboobtosi, K. Hosseinzadeh, and D.J.I.J.o.T. Ganji, Investigating the convective flow of ternary hybrid nanofluids and single nanofluids around a stretched cylinder: parameter analysis and performance enhancement, 100752 (2024).
[26] M. Haque and M.J.I.J. o. T. Alam, Natural convective heat transfer of Al2O3-Cu/water hybrid nanofluid in a rectotrapezoidal enclosure under the influence of periodic magnetic field. 22, 100661 (2024).
[27] M.S. Islam, S. Islam, and M.N.-A.-A.J.I.J. o.T. Siddiki, Numerical simulation with sensitivity analysis of MHD natural convection using Cu-TiO2-H2O hybrid nanofluids. 20, 100509 (2023).
[28] A.M.J. Al-Zamily, Analysis of natural convection and entropy generation in a cavity filled with multi-layers of porous medium and nanofluid with a heat generation, Int. J. Heat. Mass Transf. 106 (2017) 1218–1231, https://doi.org/10.1016/j.ijheatmasstransfer.2016.10.102.
[29] M. Hemmat Esfe, M. Bahiraei, H. Hajbarati, M. Valadkhani, A comprehensive review on convective heat transfer of nanofluids in porous media: energy-related and thermohydraulic characteristics, Appl. Therm. Eng. 178 (2020) 115487, https://doi.org/10.1016/j.applthermaleng.2020.115487.
[30] Z.H. Khan, W.A. Khan, M.A. Sheremet, Enhancement of heat and mass transfer rates through various porous cavities for triple convective-diffusive free convection, Energy 201 (2020) 117702, https://doi.org/10.1016/j.energy.2020.117702.
[31] V.M. Vijaya Kumara, Aswatha, K.N. Seetaramu, Finite element analysis for free convection with in porous trapezoidal cavity, Mater. Today: Proc. 52 (2022) 1633–1638, https://doi.org/10.1016/j.matpr.2021.11.276.
[32] M.A. Alomari, et al., Numerical analysis to investigate the effect of a porous block on MHD mixed convection in a split lid-driven cavity with nanofluid, Int. J. Thermofluids 22 (2024) 100621, https://doi.org/10.1016/j.ijft.2024.100621.
[33] M.A. Alomari, et al., Magnetohydrodynamic mixed convection in lid-driven curvilinear enclosure with nanofluid and partial porous layer, J. Magn. Magn. Mater. 582 (2023) 170952, https://doi.org/10.1016/j.jmmm.2023.170952.
[34] F. Selimefendigil, H.F. Öztop, Magnetohydrodynamics forced convection of nanofluid in multi-layered U-shaped vented cavity with a porous region considering wall corrugation effects, Int. Commun. Heat Mass Transf. 113 (2020) 104551, https://doi.org/10.1016/j.icheatmasstransfer.2020.104551.
[35] B. Pekmen Geridonmez, H.F. Oztop, Natural convection in a cavity filled with porous medium under the effect of a partial magnetic field, Int. J. Mech. Sci. 161-162 (2019) 105077, https://doi.org/10.1016/j.ijmecsci.2019.105077.
[36] M. Hemmat Esfe, R. Barzegarian, M. Bahiraei, A 3D numerical study on natural convection flow of nanofluid inside a cubical cavity equipped with porous fins using two-phase mixture model, Adv. Powder Technol. 31 (6) (2020) 2480–2492, https://doi.org/10.1016/j.apt.2020.04.012.
[37] F. Keramat, A. Azari, H. Rahideh, M. Abbasi, A CFD parametric analysis of natural convection in an H-shaped cavity with two-sided inclined porous fins, J. Taiwan. Inst. Chem. Eng. 114 (2020) 142–152, https://doi.org/10.1016/j.jtice.2020.09.011.
[38] M. Siavashi, R. Yousofvand, S. Rezanejad, Nanofluid and porous fins effect on natural convection and entropy generation of flow inside a cavity, Adv. Powder Technol. 29 (1) (2018) 142–156, https://doi.org/10.1016/j.apt.2017.10.021.
[39] M. Gnanasekaran, A. Satheesh, Numerical simulation of MHD double-diffusive mixed convection in a closed cavity filled with liquid potassium alloy: incorporating thermosolutal source, Case Stud. Therm. Eng. 52 (2023) 103772, https://doi.org/10.1016/j.csite.2023.103772.
[40] A. Mirzaei, P. Jalili, M.D. Afifi, B. Jalili, D.D. Ganji, Convection heat transfer of MHD fluid flow in the circular cavity with various obstacles: finite element approach, Int. J. Thermofluids 20 (2023) 100522, https://doi.org/10.1016/j.ijft.2023.100522.
[41] M. Rajarathinam, M. Akermi, M.I. Khan, N. Nithyadevi, MHD mixed convection heat transfer of copper water nanofluid in an inclined porous cavity having isothermal solid block, J. Magn. Magn. Mater. 593 (2024) 171845, https://doi.org/10.1016/j.jmmm.2024.171845.
[42] T. Saha, T. Islam, S. Yeasmin, N. Parveen, Thermal influence of heated fin on MHD natural convection flow of nanofluids inside a wavy square cavity, Int. J. Thermofluids 18 (2023) 100338, https://doi.org/10.1016/j.ijft.2023.100338.
[43] S. Ahmad, B.M. Cham, D. Liu, S.U. Islam, M.A. Hussien, H. Waqas, Numerical analysis of heat and mass transfer of MHD natural convection flow in a cavity with effects of source and sink, Case Stud. Therm. Eng. 53 (2024) 103926, https://doi.org/10.1016/j.csite.2023.103926.
[44] B.S. Reddy and S.H.S.J.P.D.E.i.A.M. Naik, Radiation, absorption, and Joule heating Influence on MHD Casson fluid flow over an exponentially stretching surface, 100790 (2024).
[45] M. Bahmani, M. Babagoli, P. Jalili, B. Jalili, and D.D.J.J.o.E.R. Ganji, The numerical study on the MHD natural convection trend of square/circle corrugated porous media, (2024).
[46] N.E.J. Asha and M.M.J.H. Molla, MRT-lattice Boltzmann simulation of MHD natural convection of Bingham nanofluid in a C-shaped enclosure with response surface analysis. 9 (12) (2023).
[47] S. Tasnim, A. Mitra, H. Saha, M.Q. Islam, and S.J.R.i.E. Saha, MHD conjugate natural convection and entropy generation of a nanofluid filled square enclosure with multiple heat-generating elements in the presence of Joule heating. 17, 100993 (2023).
[48] M. Uddin, O.Anwar Bég, and M.J.J.o.A.E. Uddin, Multiple slips and variable transport property effect on magnetohydromagnetic dissipative thermosolutal convection in a porous medium. 29 (5), 04016024 (2016).
[49] P. Patil, S. Benawadi, and E.J.C.S.i.T.E. Momoniat, Thermal analysis of bioconvective nanofluid flow over a sphere in presence of multiple diffusions and a periodic magnetic field. 51, 103569 (2023).
[50] M.K. Nayak, A.S. Dogonchi, and A.J.C.S.i.T.E. Rahbari, Free convection of Al2O3-water nanofluid inside a hexagonal-shaped enclosure with cold diamond-shaped obstacles and periodic magnetic field. 50, 103429 (2023).
[51] B.P. Geridonmez, H.J.J.o.M. Oztop, and M. Materials, Conjugate natural convection flow of a nanofluid with oxytactic bacteria under the effect of a periodic magnetic field. 564, 170135 (2022).
[52] M.N. Huda, M.S. Alam, and S.C.J.I.J.o.T. Hossain, Thermal performance investigation of transient natural convective nanofluid flow in a square cavity with inclined periodic magnetic field. 21, 100540 (2024).

[53] K. He, Y. Zhao, and L.J.I.J.o.M.F. Wang, Numerical investigation on electrohydrodynamic enhancement of solid–liquid phase change in three-dimensional cavities. 168, 104562 (2023).
[54] X.-L. Gao, J. Wu, K. Luo, H.-L. Yi, H.-P.J.I.C.i.H. Tan, and M. Transfer, Lattice Boltzmann analysis of conjugate heat transfer in the presence of electrohydrodynamic flow. 132, 105878 (2022).
[55] N.C. Roy, L.K. Saha, S.J.I.C.i.H. Siddiqa, and M. Transfer, Electrohydrodynamics and thermal radiation effects on natural convection flow in an enclosed domain. 126, 105437 (2021).
[56] M. Sheikholeslami, T. Hayat, A. Alsaedi, MHD free convection of Al2O3–water nanofluid considering thermal radiation: a numerical study, Int. J. Heat. Mass Transf. 96 (2016) 513–524.
[57] M.J. Uddin, O.A. Bég, A.I.J.J. o. t. Ismail, and h. transfer, Radiative convective nanofluid flow past a stretching/shrinking sheet with slip effects. 29 (3), 513–523 (2015).
[58] M. Usman, Z. Khan, M.J.P.A.S.M. Liu, and I. Applications, MHD natural convection and thermal control inside a cavity with obstacles under the radiation effects. 535, 122443 (2019).
[59] M. Sheikholeslami, A.J.I.J.o.H. Ghasemi, and M. Transfer, Solidification heat transfer of nanofluid in existence of thermal radiation by means of FEM. 123, 418–431 (2018).
[60] M. Ghalambaz, A. Doostani, E. Izadpanahi, A.J. Chamkha, Conjugate natural convection flow of Ag–MgO/water hybrid nanofluid in a square cavity, J. Therm. Anal. Calorim. 139 (2020) 2321–2336.
[61] M.A. Alomari, et al., Magnetohydrodynamic mixed convection in lid-driven curvilinear enclosure with nanofluid and partial porous layer, J. Magn. Magn. Mater. (2023) 170952.
[62] P. Mondal, T.J.I.J. o. M. S. Mahapatra, MHD double-diffusive mixed convection and entropy generation of nanofluid in a trapezoidal cavity, Int. J. Mech. Sci. 208 (2021) 106665.
[63] K. Vafai, C.L. Tien, Boundary and inertia effects on flow and heat transfer in porous media, Int. J. Heat. Mass Transf. 24 (2) (1981) 195–203.
[64] T. Basak, S. Roy, T. Paul, I. Pop, Natural convection in a square cavity filled with a porous medium: effects of various thermal boundary conditions, Int. J. Heat. Mass Transf. 49 (7–8) (2006) 1430–1441.
[65] Z. Du, E. Bilgen, Natural convection in vertical cavities with internal heat generating porous medium, Wärme-und Stoffübertragung 27 (3) (1992) 149–155.
[66] A. Bejan and J. Kestin, Entropy generation through heat and fluid flow, (1983).
[67] N.Z. Khan, S. Bilal, L. Kolsi, A. Shflot, and M.J.C.S.i.T.E. Malik, A case study on entropy generation in MHD nanofluid flow in l-shaped triangular corrugated permeable enclosure. 59, 104487 (2024).
[68] M.A. Alomari, K. Al-Farhany, A.L. Hashem, M.F. Al-Dawody, F. Redouane, O. A. Olayemi, Numerical study of MHD natural convection in trapezoidal enclosure filled with (50% MgO-50% Ag/Water) hybrid nanofluid: heated sinusoidal from below, Int. J. of Heat & Technology 39 (4) (2021).
[69] M.H. Esfe, A.A.A. Arani, M. Rezaie, W.-M. Yan, A. Karimipour, Experimental determination of thermal conductivity and dynamic viscosity of Ag–MgO/water hybrid nanofluid, Int. Commun. Heat Mass Transf. 66 (2015) 189–195.
[70] C.-L. Chen, C.-H. Cheng, Experimental and numerical study of mixed convection and flow pattern in a lid-driven arc-shape cavity, Heat Mass Transf. 41 (2004) 58–66.